

## Effect of Coulomb interaction on the transient optical response of electrons in field-coupled quantum dots

Xuejun Lu <sup>1</sup>, Danhong Huang <sup>2,\*</sup> and Shanhui Fan <sup>3</sup>

<sup>1</sup>*Department of Electrical & Computer Engineering, Francis College of Engineering, University of Massachusetts Lowell, Lowell, Massachusetts 01854, USA*

<sup>2</sup>*US Air Force Research Laboratory, Space Vehicles Directorate (AFRL/RVSU), Kirtland Air Force Base, New Mexico 87117, USA*

<sup>3</sup>*Ginzton Laboratory and Department of Electrical Engineering, Stanford University, Stanford, California 94305, USA*



(Received 6 November 2020; accepted 19 March 2021; published 5 April 2021)

In this work, we develop a physically transparent Coulomb-interaction model from simplification of a general many-body theory and apply this model to study interacting electron dynamics for transient occupation and quantum coherence in both single and double quantum dots under laser irradiation. Our theory considers self-consistently the Coulomb-renormalized Rabi coupling to light by using an induced optical-depolarization field, corresponding to dynamical exchange interaction between two electrons within the same quantum dot. Meanwhile, we employ evanescent-field coupling for dynamical Coulomb interaction between two electrons in different quantum dots based on a surface-plasmon model. In particular, we explore the quantum interference between a pair of laser-induced quantum coherence in three-level quantum-dot systems, which gives rise to indirect transition of electrons for sum- and difference-frequency transient optical responses. By varying laser frequency detuning, the control of laser-dressed electronic states becomes possible and can be utilized for switching among off-state, partial, and complete on-states. This study will be useful for controlling the phase entanglement of two laser-dressed states of quantum dots, as well as for enhancing the electro-optical performance through sum- and difference-frequency transitions in many optoelectronic devices.

DOI: [10.1103/PhysRevA.103.043504](https://doi.org/10.1103/PhysRevA.103.043504)

### I. INTRODUCTION

The electronic properties of a material depend on both band structures and nonequilibrium occupations of electronic states. For example, one can compute the band structure of crystal electrons accurately by using the Kohn-Sham density-functional theory [1]. Simultaneously, one can also determine the nonequilibrium occupations of crystal electrons with quantum kinetic theory [2–5], in which the Coulomb interaction between two electrons plays a crucial role on effective mass, group velocity and dynamical screening, as well as on energy relaxation of nonthermal electron distributions. One can include the retarded Coulomb interaction by using many-body theory [6] with diagrammatic-expansion technique. Interestingly, the same retarded Coulomb interaction can also be taken into account by solving coupled Maxwell-semiconductor Bloch equations [4,5,7], with which one finds the macroscopic optical-polarization field through a quantum-statistical average of the microscopic field-induced quantum coherence. Meanwhile, the quantum coherence itself is decided self-consistently from the semiconductor Bloch equations (SBE) [8–14], involving a total electric field obtained from Maxwell equations with both transverse and longitudinal optical-polarization fields [15]. The field-electron interactions, with higher-order harmonics of the total electric

field [7], can be viewed as various terms in the diagrammatic expansion [6].

The induced quantum coherence between two optically coupled electronic states of a quantum dot appears with laser frequency in resonance with two energy levels [14]. If two quantum dots stay next to each other, the quantum coherence in one interacting dot can be transferred to another noninteracting dot by a plasmon field. Similarly, if three energy levels exist in a quantum dot, the interference of direct quantum coherence [16] between lower- and upper-two energy levels gives rise to an indirect quantum coherence between the ground and top energy levels. Historically, quantum interference has been used for demonstrating lasing without inversion [17–20] and electromagnetically induced transparency [21–24] in atomic and solid-state systems. The quantum interference also leads to sum- and difference-frequency transient optical responses [25] without requiring noninversion symmetry and phase matching compared to second-order harmonic generation [26,27] in nonlinear crystals.

For an interacting spherical quantum dot, a polarization field occurs within the sphere [28], as described by a quantum-dot dielectric function [29]. Outside the sphere, an evanescent electric field exists [14]. If two quantum dots are close enough within the decay length, they become coupled to each other. One knows that the visible localized surface-plasmon (LSP) field acquires an x-ray wavelength [30], implying a subwavelength resolution for LSP. To facilitate double-dot on and off states, we introduce a dot-embedded optical nanocavity [31],

\*danhong.huang@us.af.mil

which has demonstrated large single-molecule fluorescence enhancements [32] due to greatly enhanced LSP field within the cavity. For two identical dots, there exist three states in a configuration space. The first one is an off state having two noninteracting dots. The second one is a partial-on state having one interacting dot passing its coupling to another noninteracting dot. The last one is a fully on state with two interacting dots. These three states can be switched from one to another by scanning nodes of a cavity with adjustable cavity length under resonance. This cavity-controlled switching is possible with a dynamical laser-dressing process [33,34], whereas its state reading is fulfilled by microdetection of luminescence [35] or tunneling current [36]. The cavity-field spatial distribution is computed by transfer-matrix approach and electrodynamics [28] as a generalization of geometric-optics principle [37].

The occupations of two energy levels of a dot exhibit Rabi oscillations under a resonant laser excitation. For a specific choice of modulation profile, e.g., a resonator, one finds direction-dependent Rabi-split Floquet eigenstates, resulting in direction-dependent dissipation and nonreciprocal transmission of waves [38]. Under femtosecond-laser comb excitations [39,40], the level occupations display a fast and controllable switching between two states. With a LSP nanoantenna, one can extend current research to modifying phase entanglement of two laser-dressed dots, quantum dot single- [41] or entangled-photon [42] emitters, and quantum-dot tunneling photodetectors [43]. Meanwhile, the same technique can also be applied to greatly enhance the sensitivity of infrared optoelectronics devices [44].

Semiconductor Bloch equations for interacting electrons with a laser field have been developed [8–14], including Hartree-Fock and excitonlike corrections to kinetic energies of electrons. Particularly, the correction from exchange interaction to Rabi coupling was taken into account. Moreover, generalized coupled Maxwell-semiconductor Bloch equations have also been established [4,5,7], which revealed that the Coulomb interaction between quantum wires could be viewed as the back action from an induced optical-polarization field. Here, we employ early works [4,5,7–14] and apply them to quantum-dot systems, in which both corrections to kinetic energy and Boltzman-type scatterings have been neglected for simplicity. Meanwhile, we also simplify the polarization field as a spatially homogeneous one, different from a general many-body theory [4,5,7–14]. This provides a transparent analysis for the Coulomb-interaction effect on transient optical response of electrons in interacting quantum dots. Furthermore, the current model also enables investigating complex time-dependent electron dynamics driven by a multifrequency laser pulse or laser comb, which becomes very useful for experimentally studying transient optoelectronic properties of semiconductors.

The rest of the paper is organized as follows. In Sec. II, we present density-matrix theory (DMT) for a two-level quantum-dot system including the self-consistent depolarization field for dynamical Coulomb interaction (DCI) between electrons. Moreover, we generalize this theory to a three-level DMT in Sec. III, considering the quantum interference in indirect transitions of electrons for sum- and difference-frequency transient optical responses. Section IV is for the study of

interdot DCI of electrons and its role in switching between quantum-dot on and off states by LSP coupling. Finally, conclusions and remarks are given in Sec. V.

## II. TWO-LEVEL QUANTUM-DOT SYSTEMS

We start by directly writing down the optical Bloch equations for density operator  $\hat{\rho}(t) \equiv \{\rho_{ij}\}_{2 \times 2}$  of electrons in a two-level quantum-dot system, yielding

$$\begin{aligned} \frac{d\tilde{\rho}_{12}(t|\omega)}{dt} &= \frac{1}{i\hbar}[\hbar(\omega + i\gamma_0) - (E_2 - E_1)]\tilde{\rho}_{12}(t|\omega) \\ &\quad - \frac{1}{i\hbar}[\rho_{11}(t) - \rho_{22}(t)]V_{12}^{(0)}, \\ \frac{d\rho_{22}(t)}{dt} &= -\frac{d\rho_{11}(t)}{dt} = \frac{2V_{12}^{(0)}}{\hbar} \text{Im}[\tilde{\rho}_{12}(t|\omega)], \end{aligned} \quad (1)$$

where we assume the light-electron interaction as  $V_{12}(t) = V_{12}^{(0)} \exp[i(\omega + i\gamma_0)t]$  with laser frequency  $\omega$  and dephasing rate  $\gamma_0$  and find  $\rho_{12}(t) = \tilde{\rho}_{12}(t|\omega) \exp[i(\omega + i\gamma_0)t]$ . Meanwhile, we write  $\tilde{\rho}_{21}(t|\omega) = \tilde{\rho}_{12}^*(t|\omega)$  within the rotating-wave frame. In Eq. (1),  $V_{12}^{(0)} = d_{12} \mathcal{E}_0$  with  $d_{12}$  and  $\mathcal{E}_0$  as the dipole moment of a quantum dot and the amplitude of laser field, respectively.  $E_{1,2}$  in Eq. (1) represent two energy levels of electrons.

It is well known that when light is incident on a semiconductor, its energetic photons can elevate electrons from a lower valence band to an upper conduction band, leaving many free electron-hole pairs in the system [14]. Simultaneously, its electric-field component will further move aside these negatively (positively) charged electrons (holes) in opposite spatial directions. Then, the remaining question is, do these photogenerated electrons or holes exert an action back on the photons of incident light? The answer to this lies in the induced optical-polarization field as a collection of induced dipole moments from spatial separation (interband) or charge-density waves (intra-band) of electrons and holes [15]. More importantly, this induced optical-polarization field can act back on holes and electrons, leading to a quantum-mechanical DCI between two electrons or holes, as well as one electron and hole [7]. Here, we will employ this transparent physics picture to treat the DCIs between electrons either within the same dot or in different dots, where the role of holes is replaced by a uniform background of positively charged lattice ions.

Here, we consider an ensemble of many quantum dots, which are optically isolated from each other, and each dot behaves independently for its interaction with incident light. As a result, the total optical response is the sum of contributions from each dot. The full treatment of DCI was described in details early by employing SBE [8], which can be derived from a general many-body theory but involves heavy numerical computations. The specific SBE expressions [14] for a quantum-dot system was also presented explicitly. The main focus of the current paper is developing an analytical approach for treating the DCI in optical Bloch equations, which becomes important for considering optical properties of semiconductor quantum dots. In particular, we present in this paper a transparent and intuitive formalism [15], which takes into account the DCI through an induced polarization

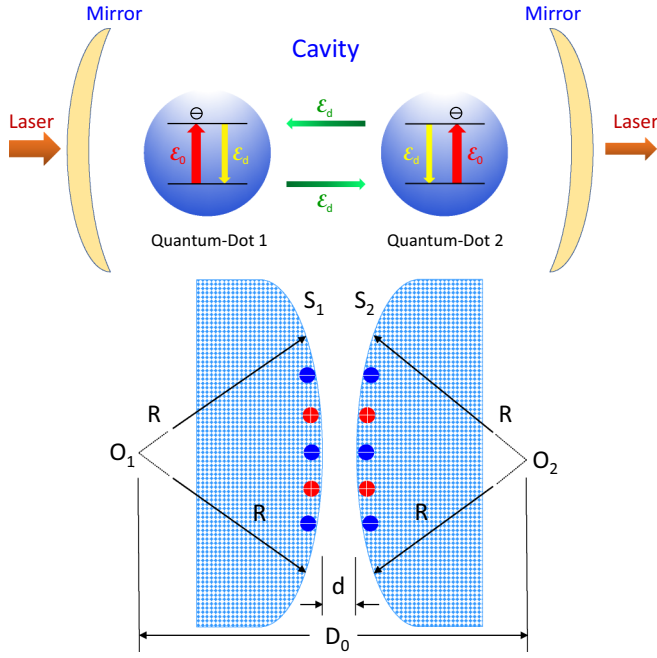


FIG. 1. (Top) Schematics of two coupled quantum dots embedded within an optical cavity under laser irradiation with frequency  $\omega$ , where  $\mathcal{E}_0$  is the laser field (red) while  $\mathcal{E}_d(\omega)$  represents the induced dynamical depolarization fields either within (yellow) or between (green) quantum dots. Each quantum dot is described by a two-level model. (Bottom) Two very close quantum dots, which center at  $O_1$  and  $O_2$  with a distance  $D_0$  and acquire two surfaces  $S_1$  and  $S_2$  with parallel tangential planes and separation  $d$ , are electromagnetically coupled to each other through induced spherical localized-surface-plasmon modes, where  $R \gg D_0 - 2R \equiv d$  is assumed, and therefore these two coupled surfaces can be approximately treated as two extremely close and parallel conducting planes.

field resulted from collective excitation of electrons in the long-wavelength limit for a single quantum dot. For double quantum dots, however, the interdot Coulomb interaction should be given by a wave-number  $q$ -dependent exponentially decayed form  $\propto \exp(-qd)$  with respect to interdot distance  $d$ .

In the presence of a laser field, electron distribution inside a quantum dot will be polarized, as illustrated in the top panel of Fig. 1, giving rise to an optical depolarization  $\tilde{\mathcal{P}}_d(t)$ . Explicitly, we can write down [14,45]

$$\tilde{\mathcal{P}}_d(t) = -n_d d_{12} \tilde{\rho}_{12}(t | \omega), \quad (2)$$

where  $n_d = f_0 n_e$  for the effective volume density of dipoles,  $f_0$  stands for the ratio of the total quantum-dot volume to the host-material volume, whereas  $n_e$  is number of electrons per quantum-dot volume. The optical depolarization in Eq. (2) corresponds to a self-consistent induced depolarization field (SCIDF) [7,45],  $\tilde{\mathcal{E}}_d(t) = \tilde{\mathcal{P}}_d(t)/\epsilon_0 \epsilon_d$ , and corrects the Rabi coupling energy  $V_{12}^{(0)}$  in Eq. (1) to a renormalized one [14,45]  $U_{12} = d_{12}[\mathcal{E}_0 + \tilde{\mathcal{E}}_d(t)] = V_{12}^{(0)} - (n_d d_{12}^2/\epsilon_0 \epsilon_d) \tilde{\rho}_{12}(t | \omega)$ , where  $\epsilon_0$  is the permittivity in vacuum, and  $\epsilon_d$  represents the host-material dielectric constant.

Classically, let us first consider a scenario with two charged objects separated by a short distance. For these two objects, there always exists a Coulomb interaction between them.

Equivalently, we can view this Coulomb interaction as an electric field produced by object-1, which exerts a Coulomb force on object-2 and vice versa. Meanwhile, a depolarization field will be produced within the object-2 due to the applied field from object-1, which, in turn, exerts another evanescent polarization force [15] back on object-1 in addition to a regular Coulomb force.

The above transparent physics picture applies here. From quantum mechanics, we know that there always exists a Coulomb interaction between two identical electrons. By using the above classical analogy, the back action here plays the role of Coulomb interaction between two electrons within the ladder approximation [14,46], which can modify the Rabi coupling energy of laser-driven electrons, i.e., the replacement of  $V_{12}^{(0)}$  by  $U_{12}$  for Coulomb renormalization.

Finally, by including this renormalization to  $V_{12}^{(0)}$ , the well-known Eq. (1) can be generalized to

$$\begin{aligned} \frac{d\tilde{\rho}_{12}(t | \omega)}{dt} &= \frac{1}{i\hbar} [\hbar(\omega + i\gamma_0) - (E_2 - E_1)] \tilde{\rho}_{12}(t | \omega) \\ &\quad - \frac{1}{i\hbar} [\rho_{11}(t) - \rho_{22}(t)] \\ &\quad \times [V_{12}^{(0)} - (n_d d_{12}^2/\epsilon_0 \epsilon_d) \tilde{\rho}_{12}(t | \omega)], \\ \frac{d\rho_{22}(t)}{dt} &= \frac{2}{\hbar} \text{Im} \{ [V_{12}^{(0)} - (n_d d_{12}^2/\epsilon_0 \epsilon_d) \tilde{\rho}_{12}^*(t | \omega)] \tilde{\rho}_{12}(t | \omega) \} \\ &= \frac{2V_{12}^{(0)}}{\hbar} \text{Im}[\tilde{\rho}_{12}(t | \omega)], \\ \rho_{11}(t) &= 1 - \rho_{22}(t), \end{aligned} \quad (3)$$

which becomes nonlinear [7] with respect to the off-diagonal density-matrix element  $\tilde{\rho}_{12}(t | \omega)$ .

Here, we would like to emphasize that the renormalization of electron kinetic energy by Hartree interaction can also be included by solving Poisson's equation, in which a density function [46], involving the diagonal density-matrix elements  $\rho_{11}(t)$  and  $\rho_{22}(t)$ , should be employed. However, the difference in kinetic-energy renormalizations between two energy levels is very small and can be neglected here or formally included in laser-frequency detuning.

Interestingly, we find from the first equation of Eq. (3) that the Coulomb-renormalized Rabi coupling can be formally absorbed into bare kinetic energy terms of electrons, yielding

$$\begin{aligned} \frac{d\tilde{\rho}_{12}(t | \omega)}{dt} &= \frac{1}{i\hbar} [\hbar(\omega + i\gamma_0) - [\tilde{E}_2(t) - \tilde{E}_1(t)]] \tilde{\rho}_{12}(t | \omega) \\ &\quad - \frac{1}{i\hbar} [\rho_{11}(t) - \rho_{22}(t)] V_{12}^{(0)}, \end{aligned} \quad (4)$$

where two time-dependent renormalized energies  $\tilde{E}_{1,2}(t)$  of electrons are defined as

$$\begin{aligned} \tilde{E}_1(t) &= E_1 - \left( \frac{n_d d_{12}^2}{\epsilon_0 \epsilon_d} \right) \rho_{11}(t), \\ \tilde{E}_2(t) &= E_2 - \left( \frac{n_d d_{12}^2}{\epsilon_0 \epsilon_d} \right) \rho_{22}(t), \end{aligned} \quad (5)$$

which resemble Fock-energy corrections. However, such a simple correspondence does not apply to the quantum-dot system addressed in Sec. III. Although the interdot Coulomb-renormalized Rabi coupling can still be absorbed into bare

kinetic energy terms of electrons in Eq. (17), an additional interdot pumping term appears for occupations. Here, we emphasize that the light-electron interaction still drives the quantum system although the Coulomb-renormalized Rabi coupling can be incorporated into electron kinetic energies, which implies the appearance of Rabi oscillations for electron occupations in the system.

In our following calculations, we will neglect dephasing effect by letting  $\gamma_0 \rightarrow 0$ . By setting  $U_{12} \rightarrow V_{12}^{(0)}$ , we know from Eq. (3) that  $\tilde{\rho}_{12}(t|\omega)$  will acquire a phase factor  $\exp(-i\delta t)$  from the first term on the right-hand side of the equation for  $d\tilde{\rho}_{12}(t|\omega)/dt$ , where  $\delta = [\hbar\omega - (E_2 - E_1)]/\hbar$  denotes the laser-frequency detuning. On the other hand, the second term on the right-hand side of the equation for  $d\tilde{\rho}_{12}(t|\omega)/dt$  in Eq. (3) leads to Rabi oscillations with respect to both  $d^2\tilde{\rho}_{12}(t|\omega)/dt^2$  and  $d^2[\rho_{11}(t) - \rho_{22}(t)]/dt^2$ . Interestingly, the SCIDF has no effect on the pumping of electrons between two energy levels, which is driven only by external laser field.

Physically, we can gradually turn on a laser field at time  $t_0$  so as to use initial conditions  $\rho_{11}(0) = 1$  and  $\rho_{22}(0) = 0$ . Mathematically, such a turning-on process can be simulated by introducing a broadened step function  $S_0(t)$ , given by

$$S_0(t) = \frac{1}{2} + \frac{1}{\pi} \tan^{-1} \left( \frac{t - t_0}{\Gamma_0} \right), \quad (6)$$

which approaches zero if  $(t - t_0)/\Gamma_0 \ll -1$  or unity for  $(t - t_0)/\Gamma_0 \gg 1$ , where positive  $\Gamma_0 \ll t_0$  represents broadening in a step function. Meanwhile, we should also set positive turning-on time  $t_0$  far away from zero to ensure the accuracy of initial conditions in the absence of optical field. Therefore, we will replace  $V_{12}^{(0)} = d_{12}\mathcal{E}_0$  by  $d_{12}\mathcal{E}_0 S_0(t)$ . Furthermore, we would solve Eq. (3) using  $U_{12}(t) = d_{12}\mathcal{E}_0 S_0(t) - (n_d d_{12}^2/\epsilon_0\epsilon_d) \tilde{\rho}_{12}(t|\omega)$ .

According to the Kane approximation [14], the dipole moment  $d_{12} = d_{cv}$  for electrons in a quantum dot between the valence and conduction bands at the isotropic  $\Gamma$  point is calculated as

$$d_{cv} = \sqrt{\frac{e^2\hbar^2}{2m_0E_G} \left( \frac{m_0}{m^*} - 1 \right)}, \quad (7)$$

where  $m^*$  and  $E_G$  are the effective mass of electrons and the bandgap of host material for a quantum dot, and  $m_0$  is the free-electron mass.

On the other hand, for the dipole moment  $d_{12}$  of electrons within the conduction band at the  $\Gamma$  point, we employ the harmonic-oscillator model for a quantum dot. As a result, we obtain the dipole moment  $d_{n,n+1}$  between two energy levels  $E_n = (n - 1/2)\hbar\omega_0$  and  $E_{n+1} = (n + 1/2)\hbar\omega_0$  with  $n = 1, 2, \dots$ , yielding [6]

$$d_{n,n+1} = er_0 \sqrt{\frac{n}{2}}, \quad (8)$$

where  $r_0 = \sqrt{\hbar/(m^*\omega_0)}$  represents the effective radius of a quantum dot. Moreover, we find  $d_{23} = \sqrt{2}d_{12} = er_0$ , which is larger than  $d_{cv}$  in Eq. (7).

As a starting point, we would first explore the Coulomb-interaction effect for electrons within a two-level quantum dot. For steady-state electrons, we formally get the solution

of Eq. (1) as [47–52]

$$\begin{aligned} \frac{d}{dt} \{ [\rho_{11}(t) - \rho_{22}(t)]^2 + 4|\tilde{\rho}_{12}(t|\omega)|^2 \} &= 0, \\ \tilde{\rho}_{12}(t|\omega) &= \left[ \frac{\rho_{11}(t) - \rho_{22}(t)}{\hbar\omega - (E_2 - E_1)} \right] V_{12}^{(0)}. \end{aligned} \quad (9)$$

For numerical calculations in Sec. II, we set  $r_0 = 23 \text{ \AA}$ ,  $n_d = 0$  and  $n_d = 4.9 \times 10^{15} \text{ m}^{-3}$  for unrenormalized and renormalized Rabi couplings, respectively. Moreover, for the laser field with frequency  $\omega$ , we assume  $\Omega_R = |V_{12}^{(0)}|/\hbar = d_{12}\mathcal{E}_0/\hbar = 1.09 \times 10^5 \text{ Hz}$  for the Rabi frequency. The other parameters, e.g., detuning  $\delta = (\hbar\omega - E_{21})/\hbar$ , in numerical calculations will be provided directly in the figure caption.

For unrenormalized case with  $n_d = 0$ , the calculated  $\rho_{11}(t)$ ,  $\rho_{22}(t)$  and  $\text{Re}[\tilde{\rho}_{12}(t|\omega)]$  are presented in Fig. 2 as functions of time  $t$ . From Fig. 2 we find that both  $\rho_{11}(t)$  and  $\rho_{22}(t)$  in the left panel display Rabi oscillations with a time period of  $2\pi/\sqrt{\delta^2 + 4\Omega_R^2}$  for  $\delta = 2\Omega_R$ . Meanwhile, there exists a gap between the valley of  $\rho_{11}(t)$  and the peak of  $\rho_{22}(t)$ , and this gap will close as  $\delta \rightarrow 0$ . Moreover, from the right panel of Fig. 2, we observe an onset of  $\tilde{\rho}_{12}(t|\omega)$  around  $t = 0$  due to the use of  $S_0(t)$ , which is followed by Rabi oscillations of  $\tilde{\rho}_{12}(t|\omega)$  with a peak-to-valley amplitude slightly smaller than 0.5 due to  $\delta \neq 0$ .

In fact, by setting  $U_{12} \rightarrow V_{12}^{(0)}$  and neglecting the slow oscillations, proportional to  $\exp(-i\delta t)$  and  $\sin^2(\Omega_R t)$ , from detuning  $\delta$  and Rabi frequency  $\Omega_R$ , we obtain from Eq. (9) the amplitudes for Rabi oscillations in  $\tilde{\rho}_{12}(t|\omega)$  and  $\rho_{22}(t)$ , namely

$$\begin{aligned} \tilde{\rho}_{12}^{(0)}(\omega) &= \frac{\text{sgn}[\hbar\omega - (E_2 - E_1)]\hbar\Omega_R}{\sqrt{[\hbar\omega - (E_2 - E_1)]^2 + 4\hbar^2\Omega_R^2}}, \\ \rho_{22}^{(0)}(\omega) &= 1 - \rho_{11}^{(0)}(\omega) \\ &= \frac{1}{2} \left[ 1 - \frac{|\hbar\omega - (E_2 - E_1)|}{\sqrt{[\hbar\omega - (E_2 - E_1)]^2 + 4\hbar^2\Omega_R^2}} \right], \end{aligned} \quad (10)$$

where  $\text{sgn}(x)$  is the sign function. Consequently, using Eq. (10) for the steady state of electrons, we further obtain

$$\begin{aligned} \rho_{22}(t) &= \rho_{22}^{(0)} \sin^2 \left[ (t/2) \sqrt{\delta^2 + 4\Omega_R^2} \right] \\ &= \frac{1}{2} \rho_{22}^{(0)} [1 - \cos(t\sqrt{\delta^2 + 4\Omega_R^2})], \\ \rho_{11}(t) &= 1 - \rho_{22}(t) = 1 - \rho_{22}^{(0)} \sin^2 \left[ (t/2) \sqrt{\delta^2 + 4\Omega_R^2} \right] \\ &= 1 - \frac{1}{2} \rho_{22}^{(0)} [1 - \cos(t\sqrt{\delta^2 + 4\Omega_R^2})], \\ \text{Re}[\tilde{\rho}_{12}(t|\omega)] &= \frac{1}{2} - |\tilde{\rho}_{12}^{(0)}(\omega)| \sin^2 \left[ (t/2) \sqrt{\delta^2 + 4\Omega_R^2} \right] \\ &= \frac{1}{2} - \frac{1}{2} |\tilde{\rho}_{12}^{(0)}(\omega)| [1 - \cos(t\sqrt{\delta^2 + 4\Omega_R^2})], \\ \text{Im}[\tilde{\rho}_{12}(t|\omega)] &= \frac{1}{2\Omega_R} \frac{d\rho_{22}(t)}{dt} = \frac{\sqrt{\delta^2 + 4\Omega_R^2}}{4\Omega_R} \\ &\quad \times \rho_{22}^{(0)} \sin(t\sqrt{\delta^2 + 4\Omega_R^2}), \end{aligned} \quad (11)$$

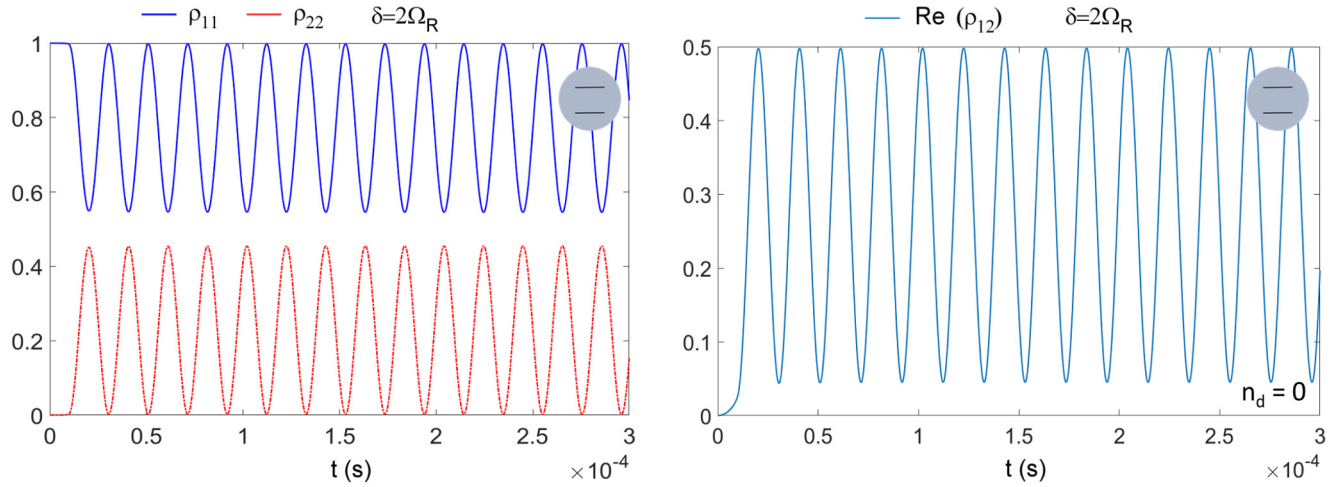


FIG. 2. Calculated occupations  $\rho_{11}(t)$  (blue solid) and  $\rho_{22}(t)$  (red dash-dotted) as functions of time  $t$  (left) and real part of the quantum coherence  $\text{Re}[\tilde{\rho}_{12}(t|\omega)]$  (right) as a function of  $t$  within the rotating-wave frame. Here, we have set  $n_d = 0$ ,  $\delta = 2\Omega_R$  for the unrenormalized case, and the periodic Rabi oscillations in the left and right panels can be seen clearly.

which fully agree with our numerical results presented in Fig. 2.

Figure 3 presents the Fourier transform (FT) of both  $\text{Re}[\tilde{\rho}_{12}(t|\omega)]$  and  $\text{Im}[\tilde{\rho}_{12}(t|\omega)]$  as functions of scaled FT frequency  $\omega/\Omega_R$ . For  $\text{Im}[\tilde{\rho}_{12}(t|\omega)]$  in the right panel, we find two spectral peaks at  $\omega = \pm\sqrt{\delta^2 + 4\Omega_R^2} = \pm 2\sqrt{2}\Omega_R$  for  $\delta = 2\Omega_R$ . These two side peaks are also seen in the left panel for  $\text{Re}[\tilde{\rho}_{12}(t|\omega)]$ , and moreover, we observe a central peak at  $\omega = 0$  due to the constant term involved in  $\text{Re}[\tilde{\rho}_{12}(t|\omega)]$ , as can be verified from Eq. (11).

As demonstrated in Ref. [14], the existence of Coulomb interaction between electrons within the same quantum dot will add a correction term to the bare Rabi coupling energy  $V_{12}^{(0)}$ , and then renormalize  $V_{12}^{(0)}$  into a new one  $U_{12}(t)$ . This renormalized one contains the induced quantum coherence  $\rho_{12}(t)$  of electrons. As a result, the corrected stimulated

transition  $\text{Im}\{U_{12}(t)\rho_{12}(t)\}$  of electrons involves a nonlinear term  $[\rho_{12}(t)]^2$  in the time domain with respect to the induced quantum coherence. Such a band-edge nonlinearity is completely different from the common optical nonlinearity [26] in crystals with no requirements for crystal symmetry and phase matching condition, and it exists only in the presence of Coulomb interaction.

In comparison with  $V_{12}^{(0)} = d_{12}\mathcal{E}_0$ , the higher-harmonic effect from the corrected  $U_{12}$  is expected to show up around peaks (but not valleys) of Rabi oscillations, where positive  $\tilde{\rho}_{12}(t|\omega)$  can take its maximum value for enhanced nonlinearity. In Fig. 4 we present calculated  $\rho_{11}(t)$ ,  $\rho_{22}(t)$ , and  $\text{Re}[\tilde{\rho}_{12}(t|\omega)]$  by including the SCIDF correction to  $\Omega_R$  for  $n_d = 4.9 \times 10^{15} \text{ m}^{-3}$ . From the left panel, we find the gap between the valley of  $\rho_{11}(t)$  and the peak of  $\rho_{22}(t)$  is slightly increased by Coulomb interaction among electrons within the

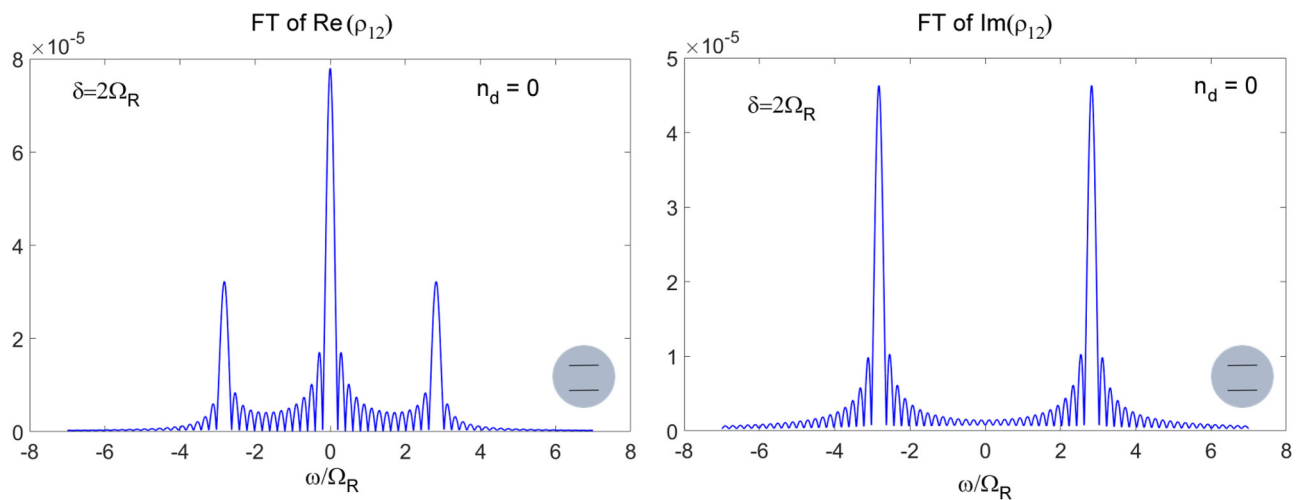


FIG. 3. Results for Fourier transform (FT) of  $\text{Re}[\tilde{\rho}_{12}(t|\omega)]$  (left) and  $\text{Im}[\tilde{\rho}_{12}(t|\omega)]$  (right) as functions of frequency  $\omega/\Omega_R$ . Here, we set  $n_d = 0$  and  $\delta = 2\Omega_R$  for the unrenormalized case. The background oscillations come from finite time windows for Fourier transform performed.

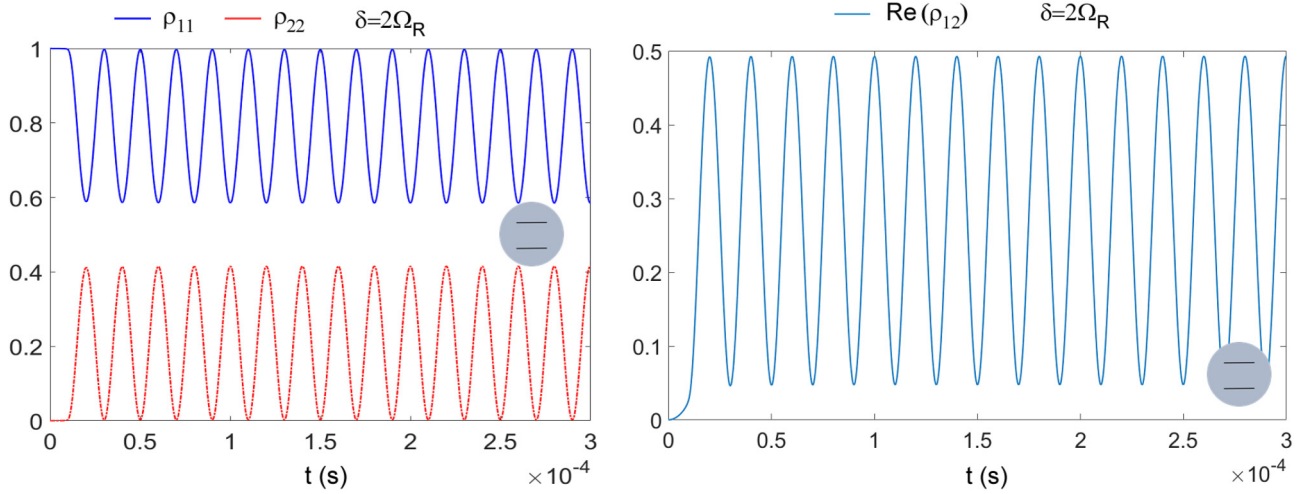


FIG. 4. Calculated occupations  $\rho_{11}(t)$  (blue solid) and  $\rho_{22}(t)$  (red dash-dotted) as functions of time  $t$  (left) and real part of the quantum coherence  $\text{Re}[\tilde{\rho}_{12}(t | \omega)]$  (right) as a function of  $t$  within the rotating-wave frame. Here, we have set  $n_d = 4.9 \times 10^{15} \text{ m}^{-3}$  and  $\delta = 2\Omega_R$  for the renormalized case, and the amplitude of Rabi oscillations in the left panel is reduced significantly.

same dot. However, this intradot Coulomb-interaction effect only plays an insignificant role in  $\text{Re}[\tilde{\rho}_{12}(t | \omega)]$ , as seen from the right panel, due to large detuning  $\delta = 2\Omega_R$ .

By increasing the intradot Coulomb interaction and reducing the detuning at the same time, we find from Fig. 5 for  $n_d = 1.8 \times 10^{16} \text{ m}^{-3}$  and  $\delta = 0.2\Omega_R$  that the gap between the valley of  $\rho_{11}(t)$  and the peak of  $\rho_{22}(t)$  in Fig. 4 disappears in the left panel. This is accompanied by the increased peak-to-valley amplitudes of  $\rho_{11}(t)$  and  $\rho_{22}(t)$  due to reduced  $\delta$ . More interestingly, the peak splitting, or equivalently the sum-frequency transient optical response (SFTOR), in  $\text{Re}[\tilde{\rho}_{12}(t | \omega)]$  appears in the right panel, which is attributed to enhanced Coulomb interaction between electrons in a quantum dot. In comparison with Fig. 3 for the unrenormalized case, the strong higher-harmonic peaks at  $\omega \approx \pm 4\omega_R$  show

up for  $\text{Re}[\tilde{\rho}_{12}(t | \omega)]$  in the left panel of Fig. 6 but are still too weak to be seen for  $\text{Im}[\tilde{\rho}_{12}(t | \omega)]$  in the right panel.

Due to the existed time periodicity in the applied optical field  $\mathcal{E}_0(t)$ , we expect the periodic feature in all elements of the density matrix in its steady states. As a result, the Fourier spectra of these elements are expected discrete. Indeed, we find discrete Fourier peaks for  $\tilde{\rho}_{12}(t | \omega)$  in Figs. 3 and 6 with respect to cases without ( $n_d = 0$ ) and with ( $n_d \neq 0$ ) Coulomb-interaction effects. In addition, we also find a weak background between these discrete Fourier peaks due to the limited time window taken in performing the Fourier transforms. Since all discrete Fourier peaks can stand out clearly, including both cases for  $n_d = 0$  and  $n_d \neq 0$ , we will not make extra effort on extending time windows for performing Fourier transforms again.

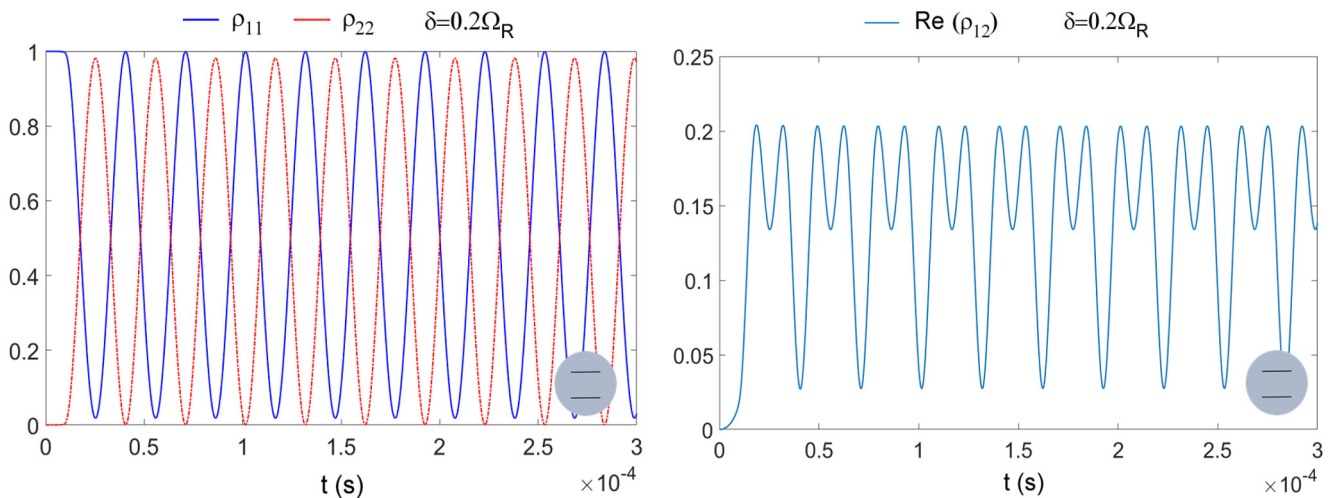


FIG. 5. Calculated occupations  $\rho_{11}(t)$  (blue solid) and  $\rho_{22}(t)$  (red dash-dotted) as functions of time  $t$  (left) and real part of the quantum coherence  $\text{Re}[\tilde{\rho}_{12}(t | \omega)]$  (right) as a function of  $t$  within the rotating-wave frame. Here, we have set  $n_d = 1.8 \times 10^{16} \text{ m}^{-3}$ ,  $\delta = 0.2\Omega_R$  for the renormalized case, and the Rabi oscillations in the left panel can be seen clearly.



In our calculations, we assume  $\mathcal{E}_3 = 0$  and  $d_{13} = 0$  due to electron transition between two states with the same parity. This leads to  $U_{13}(t) \equiv 0$  but  $\rho_{13}(t) \neq 0$ . Thus, from Eq. (12), we obtain

$$\begin{aligned}
i\hbar \frac{d\rho_{11}(t)}{dt} &= -2i \operatorname{Im}[U_{12}^*(t)\rho_{12}(t)], \\
i\hbar \frac{d\rho_{22}(t)}{dt} &= 2i \operatorname{Im}[U_{12}^*(t)\rho_{12}(t)] - 2i \operatorname{Im}[U_{23}^*(t)\rho_{23}(t)], \\
i\hbar \frac{d\rho_{33}(t)}{dt} &= -i\hbar \left[ \frac{d\rho_{11}(t)}{dt} + \frac{d\rho_{22}(t)}{dt} \right] = 2i \operatorname{Im}[U_{23}^*(t)\rho_{23}(t)], \\
i\hbar \frac{d\rho_{12}(t)}{dt} &= i\hbar \frac{d\rho_{21}^*(t)}{dt} = -(E_2 - E_1)\rho_{12}(t) - [\rho_{11}(t) - \rho_{22}(t)]U_{12}(t) - U_{23}^*(t)\rho_{13}(t), \\
i\hbar \frac{d\rho_{23}(t)}{dt} &= i\hbar \frac{d\rho_{32}^*(t)}{dt} = -(E_3 - E_2)\rho_{23}(t) - [\rho_{22}(t) - \rho_{33}(t)]U_{23}(t) + U_{12}^*(t)\rho_{13}(t), \\
i\hbar \frac{d\rho_{13}(t)}{dt} &= i\hbar \frac{d\rho_{31}^*(t)}{dt} = -(E_3 - E_1)\rho_{13}(t) + U_{12}(t)\rho_{23}(t) - U_{23}(t)\rho_{12}(t), \tag{14}
\end{aligned}$$

where  $\rho_{11}(t) + \rho_{22}(t) + \rho_{33}(t) = \text{const}$  for the conservation of total electron number.

In Eq. (14), there is no direct transition between the first and third energy levels of electrons since  $U_{13}(t) \equiv 0$ . However, a finite indirect quantum coherence  $\rho_{13}(t) \neq 0$  could still exist between these two electronic states, which is facilitated by the interference between two laser-induced quantum coherence  $\rho_{12}(t)$  and  $\rho_{23}(t)$  [16]. In particular, we can set  $\omega_1 \approx \omega_2$  if  $E_2 - E_1 \approx E_3 - E_2$ . As a result, the induced quantum coherence  $\rho_{13}(t)$  in Eq. (14) will behave in a way very similar to a direct one with frequency  $\omega_1 + \omega_2$  [25].

By writing  $E_{jj'} = E_j - E_{j'}$  and assuming  $\rho_{12}(t) = \tilde{\rho}_{12}(t) \exp(i\omega_1 t)$ ,  $\rho_{23}(t) = \tilde{\rho}_{23}(t) \exp(i\omega_2 t)$  as well as  $\rho_{13}(t) = \tilde{\rho}_{13}(t) \exp[i(\omega_1 + \omega_2)t]$ , we get from Eq. (14)

$$\begin{aligned}
i\hbar \frac{d\rho_{11}(t)}{dt} &= -2i \operatorname{Im}[\tilde{U}_{12}^*(t)\tilde{\rho}_{12}(t)], \\
i\hbar \frac{d\rho_{22}(t)}{dt} &= 2i \operatorname{Im}[\tilde{U}_{12}^*(t)\tilde{\rho}_{12}(t)] - 2i \operatorname{Im}[\tilde{U}_{23}^*(t)\tilde{\rho}_{23}(t)], \\
i\hbar \frac{d\rho_{33}(t)}{dt} &= -i\hbar \left[ \frac{d\rho_{11}(t)}{dt} + \frac{d\rho_{22}(t)}{dt} \right] = 2i \operatorname{Im}[\tilde{U}_{23}^*(t)\tilde{\rho}_{23}(t)], \\
i\hbar \frac{d\tilde{\rho}_{12}(t)}{dt} &= i\hbar \frac{d\tilde{\rho}_{21}^*(t)}{dt} = (\hbar\omega_1 - E_{21})\tilde{\rho}_{12}(t) - [\rho_{11}(t) - \rho_{22}(t)]\tilde{U}_{12}(t) - \tilde{U}_{23}^*(t)\tilde{\rho}_{13}(t), \\
i\hbar \frac{d\tilde{\rho}_{23}(t)}{dt} &= i\hbar \frac{d\tilde{\rho}_{32}^*(t)}{dt} = (\hbar\omega_2 - E_{32})\tilde{\rho}_{23}(t) - [\rho_{22}(t) - \rho_{33}(t)]\tilde{U}_{23}(t) + \tilde{U}_{12}^*(t)\tilde{\rho}_{13}(t), \\
i\hbar \frac{d\tilde{\rho}_{13}(t)}{dt} &= i\hbar \frac{d\tilde{\rho}_{31}^*(t)}{dt} = [\hbar(\omega_1 + \omega_2) - E_{31}]\tilde{\rho}_{13}(t) + \tilde{U}_{12}(t)\tilde{\rho}_{23}(t) - \tilde{U}_{23}(t)\tilde{\rho}_{12}(t), \tag{15}
\end{aligned}$$

where  $\tilde{U}_{12}(t) = d_{12} \mathcal{E}_1 \mathcal{S}_0(t) - (n_d d_{12}^2 / \epsilon_0 \epsilon_d) \tilde{\rho}_{12}(t)$  and  $\tilde{U}_{23}(t) = d_{23} \mathcal{E}_2 \mathcal{S}_0(t) - (n_d d_{23}^2 / \epsilon_0 \epsilon_d) \tilde{\rho}_{23}(t)$ . From Eq. (15) we find that finite occupation  $\rho_{33}(t)$  for the top energy level can be achieved by two consecutive optical transitions from two low-energy levels although there exists no direct optical transition from the bottom to the top energy level. At the same time, the sum-frequency quantum coherence  $\tilde{\rho}_{13}(t)$  also shows up as a consequence of quantum interference between  $\tilde{\rho}_{12}(t)$  and  $\tilde{\rho}_{23}(t)$ , leading to indirect transition of electrons as well as the sum- and difference-frequency transient optical responses due to renormalized Rabi couplings.

If we further assume  $\omega_1 = \omega_2 = \omega$  and  $E_{21} = E_{32} = \Delta E$ , we get from Eq. (15)

$$\begin{aligned}
i\hbar \frac{d\rho_{11}(t)}{dt} &= -2i \operatorname{Im}[\tilde{U}_{12}^*(t)\tilde{\rho}_{12}(t)], \\
i\hbar \frac{d\rho_{22}(t)}{dt} &= 2i \operatorname{Im}[\tilde{U}_{12}^*(t)\tilde{\rho}_{12}(t)] - 2i \operatorname{Im}[\tilde{U}_{23}^*(t)\tilde{\rho}_{23}(t)], \\
i\hbar \frac{d\rho_{33}(t)}{dt} &= -i\hbar \left[ \frac{d\rho_{11}(t)}{dt} + \frac{d\rho_{22}(t)}{dt} \right] = 2i \operatorname{Im}[\tilde{U}_{23}^*(t)\tilde{\rho}_{23}(t)], \\
i\hbar \frac{d\tilde{\rho}_{12}(t)}{dt} &= i\hbar \frac{d\tilde{\rho}_{21}^*(t)}{dt} = (\hbar\omega - \Delta E)\tilde{\rho}_{12}(t) - [\rho_{11}(t) - \rho_{22}(t)]\tilde{U}_{12}(t) - \tilde{U}_{23}^*(t)\tilde{\rho}_{13}(t), \\
i\hbar \frac{d\tilde{\rho}_{23}(t)}{dt} &= i\hbar \frac{d\tilde{\rho}_{32}^*(t)}{dt} = (\hbar\omega - \Delta E)\tilde{\rho}_{23}(t) - [\rho_{22}(t) - \rho_{33}(t)]\tilde{U}_{23}(t) + \tilde{U}_{12}^*(t)\tilde{\rho}_{13}(t), \\
i\hbar \frac{d\tilde{\rho}_{13}(t)}{dt} &= i\hbar \frac{d\tilde{\rho}_{31}^*(t)}{dt} = (2\hbar\omega - 2\Delta E)\tilde{\rho}_{13}(t) + \tilde{U}_{12}(t)\tilde{\rho}_{23}(t) - \tilde{U}_{23}(t)\tilde{\rho}_{12}(t). \tag{16}
\end{aligned}$$

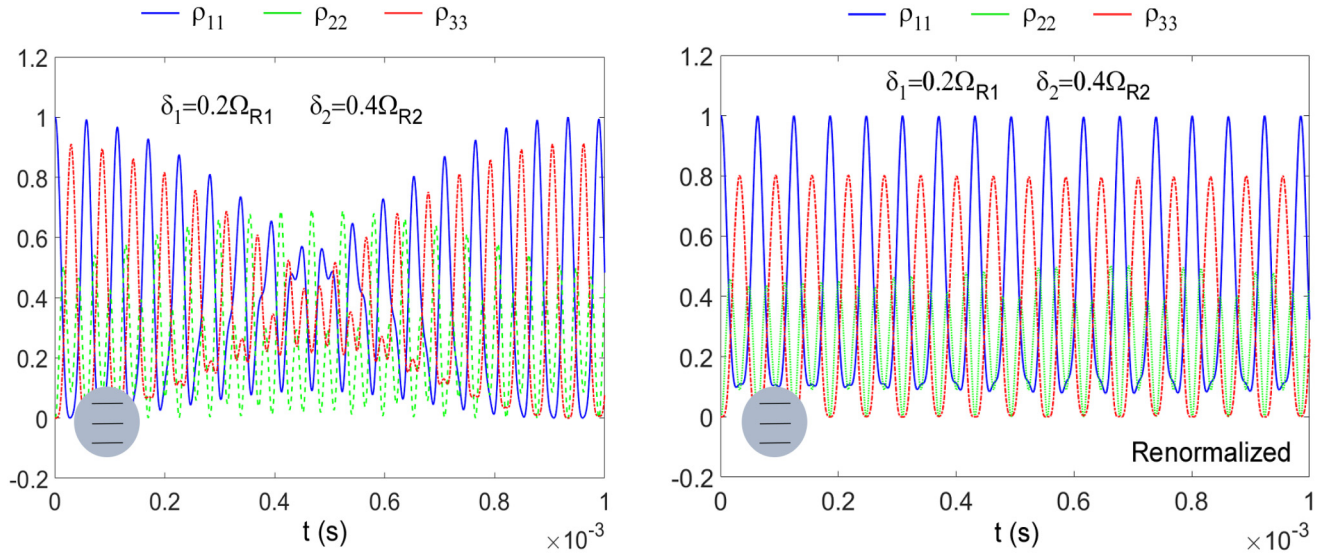


FIG. 7. Comparison of occupations  $\rho_{11}(t)$  (blue solid),  $\rho_{22}(t)$  (green short-dashed), and  $\rho_{33}(t)$  (red dash-dotted) as functions of time  $t$  with (right) and without (left) renormalized Rabi coupling for a three-level quantum dot. Here, we have set  $\rho_{11}(0) = 1$ ,  $\rho_{22}(0) = \rho_{33}(0) = 0$  as initial conditions,  $\delta_1 = 0.2 \Omega_{R1}$ , and  $\delta_2 = 0.4 \Omega_{R2}$ .

where the  $2\omega$  optical response is expected from the indirect transition of electrons between the first and third energy levels.

For numerical calculations in Sec. III, we set  $r_0 = 23 \text{ \AA}$ ,  $n_d = 0$ , and  $n_d = 1.8 \times 10^{16} \text{ m}^{-3}$  for unrenormalized and renormalized Rabi couplings, respectively. Moreover, for two laser fields with frequencies  $\omega_1$  and  $\omega_2$ , we assume  $\Omega_{R1} = \Omega_{R2}/\sqrt{2} = 1.09 \times 10^5 \text{ Hz}$  for their Rabi frequencies due to different dipole moments  $d_{12} = d_{23}/\sqrt{2}$ . The other parameters, such as  $\delta_1$ ,  $\delta_2$ , in numerical calculations will be directly indicated in the figure caption.

From Fig. 7 with small dephasing, we find slow-beating features, or equivalently the difference-frequency transient optical response (DFTOR), for occupations  $\rho_{11}(t)$  and  $\rho_{33}(t)$  in its left panel as the DCI between two electrons within the same quantum dot has been neglected. However, only the amplitude modulation is found for  $\rho_{22}(t)$  at the same time. In addition,  $\rho_{11}(t)$  reaches its maximum whenever  $\rho_{22}(t)$  and  $\rho_{33}(t)$  sit at their minima. Furthermore, the time period for oscillating  $\rho_{22}(t)$  is reduced by half compared to oscillations in  $\rho_{11}(t)$  and  $\rho_{33}(t)$ . Meanwhile, the oscillations in  $\rho_{11}(t)$  are found to be out of phase with those in  $\rho_{33}(t)$ . As the intensive intradot DCI is turned on in the right panel of Fig. 7, both DFTOR and amplitude-modulation features are suppressed, indicating the effect of Coulomb interaction between two electrons. But, the phase relations among oscillations in  $\rho_{11}(t)$ ,  $\rho_{22}(t)$ , and  $\rho_{33}(t)$  remain.

Figure 8 displays a periodic peak SFTOR for  $\text{Im}[\tilde{\rho}_{12}(t)]$  in its top-right panel with switching strength for dual peaks in the unrenormalized case, although no SFTOR occurs for  $\text{Re}[\tilde{\rho}_{12}(t)]$  at the same time in the top-left panel. However, a full DFTOR is present in the top-left panel with completing beating nodes. Here, both of these observations can be attributed to the indirect quantum coherence  $\tilde{\rho}_{13}(t)$  due to quantum-interference effect resulted from the term  $\tilde{U}_{23}^*(t) \tilde{\rho}_{13}(t)$  in Eq. (15). Once intradot DCI between electrons

has been added, the DFTOR found in the top-left panel turns into strong periodic peak SFTOR with a constant amplitude in the bottom-left panel. On the other hand, the peak-split SFTOR in the top-right panel is greatly washed out, leaving only a shoulder at the right-hand side of individual peak.

It is known from the top-right panel of Fig. 9 that a periodic peak SFTOR shows up for  $\text{Im}[\tilde{\rho}_{23}(t)]$  for the unrenormalized case but acquires a different pattern compared to the same panel in Fig. 8. This new feature also results from the indirect quantum coherence  $\tilde{\rho}_{13}(t)$  due to quantum-interference effect given by a different term  $\tilde{U}_{12}^*(t) \tilde{\rho}_{13}(t)$  in Eq. (15). Moreover, the beating nodes of  $\text{Re}[\tilde{\rho}_{12}(t)]$  in the top-left panel of Fig. 8 is found smeared out in the same panel of Fig. 9. If we take into account the effect of intradot DCI between two electrons, the peak-split SFTOR in the top-right panel of Fig. 9 has been significantly obscured for  $\text{Im}[\tilde{\rho}_{23}(t)]$  in its bottom-right panel, leaving only a shoulder at the left-hand side of individual peak in contrast to the finding in the same panel of Fig. 8. Furthermore, the incomplete DFTOR developed in the top-left panel of Fig. 9 changes into a constant-amplitude oscillation in its bottom-left panel with superposed peak-split SFTOR by intradot DCI.

In order to gain a full understanding of both sum- and difference-frequency nonlinear characters, as well as quantum-interference effects associated with indirect quantum coherence  $\tilde{\rho}_{13}(t)$ , we present  $\text{Re}[\tilde{\rho}_{13}(t)]$  and  $\text{Im}[\tilde{\rho}_{13}(t)]$  in Fig. 10 with either bare or renormalized Rabi couplings. For the unrenormalized case, we find periodic peak SFTOR and DFTOR pattern, respectively, from  $\text{Re}[\tilde{\rho}_{13}(t)]$  and  $\text{Im}[\tilde{\rho}_{13}(t)]$  in the top-left and top-right panels of Fig. 10, which is supplemented by a large modulation for the valleys of  $\text{Re}[\tilde{\rho}_{13}(t)]$ . There exists a similarity for DFTOR between  $\text{Im}[\tilde{\rho}_{13}(t)]$  and  $\text{Re}[\tilde{\rho}_{12}(t)]$  in Fig. 8 or  $\text{Re}[\tilde{\rho}_{23}(t)]$  in Fig. 9, as expected from the equation for  $d\tilde{\rho}_{13}(t)/dt$  in Eq. (15). For the renormalized case, on the other hand, the periodic peak SFTOR in the top-left panel of Fig. 10 changes into periodic valley SFTOR.



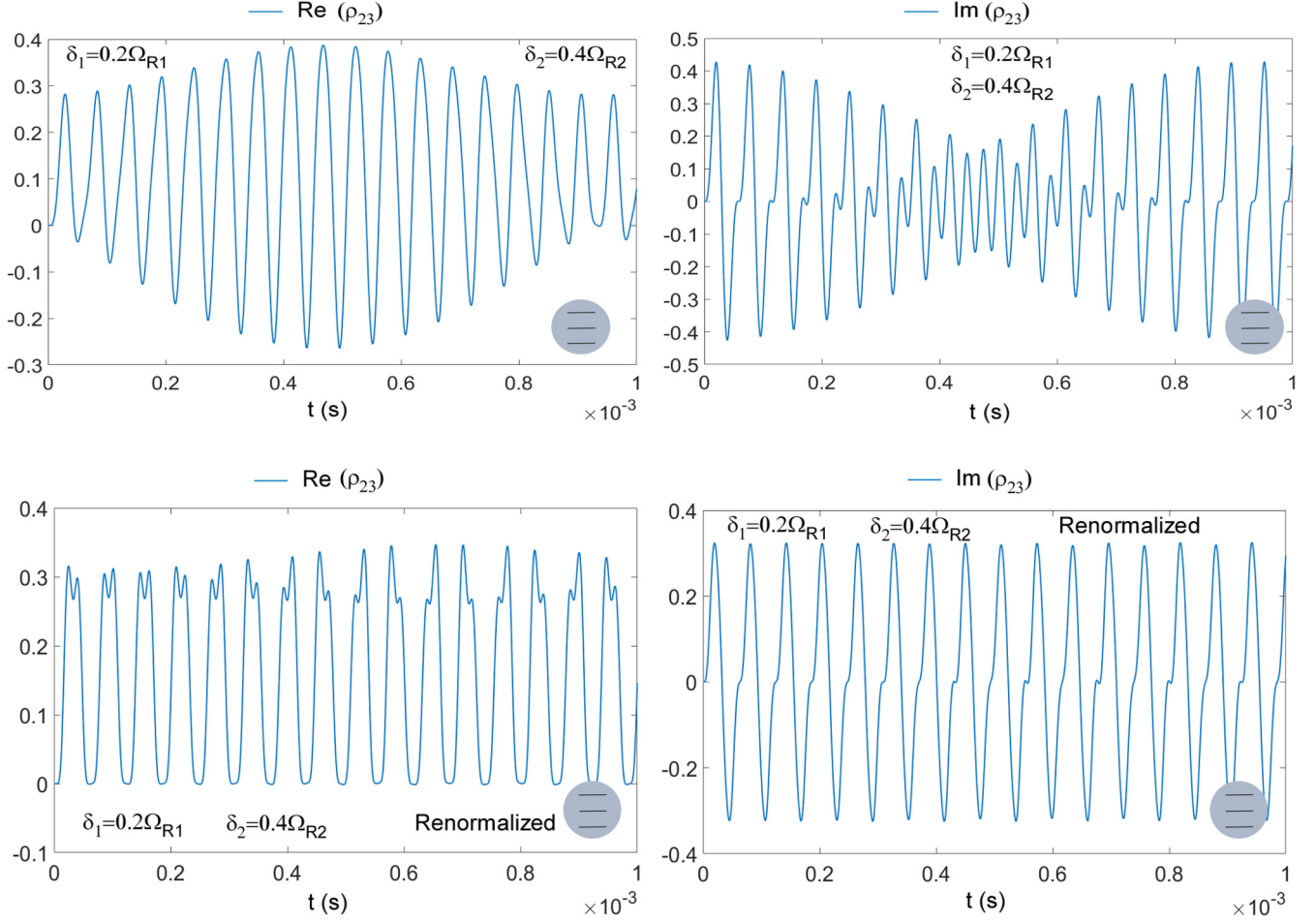


FIG. 9. Comparisons of  $\text{Re}[\tilde{\rho}_{23}(t)]$  (left) and  $\text{Im}[\tilde{\rho}_{23}(t)]$  (right) as functions of time  $t$  with (bottom) and without (top) renormalized Rabi coupling for a three-level quantum dot. Here, we have set  $\rho_{11}(0) = 1$ ,  $\rho_{22}(0) = \rho_{33}(0) = 0$  as initial conditions,  $\delta_1 = 0.2\Omega_{R1}$ , and  $\delta_2 = 0.4\Omega_{R2}$ .

Fermi energy  $E_F$  at low temperatures, i.e.,  $\rho_{jj}(0) = \Theta(E_F - E_j)$  with unity-step function  $\Theta(x)$ , where the states below the Fermi energy are occupied while those above the Fermi energy remains empty. Moreover, these electronic states can be either spin or orbital degenerate. Therefore, for two occupied states, the natural selection is  $\rho_{11}(0) = \rho_{22}(0) = 1$ ,  $\rho_{33}(0) = 0$  but not  $\rho_{11}(0) = \rho_{22}(0) = 1/2$ ,  $\rho_{33}(0) = 0$ . This is quite different from single-electron case in atomic optics.

#### IV. NEAR-FIELD COUPLED QUANTUM DOTS

Now, let us turn to a system containing two quantum dots coupled by a near field. For simplicity, we only consider a two-level model for a pair of field-coupled quantum dots, as illustrated in the bottom panel of Fig. 1. For each quantum dot, we generalize Eq. (3) to [7]

$$\begin{aligned}
 \frac{d\tilde{\rho}_{12}^{\alpha,\beta}(t|\omega)}{dt} &= \frac{1}{i\hbar} [\hbar\omega - (E_2^{\alpha,\beta} - E_1^{\alpha,\beta})] \tilde{\rho}_{12}^{\alpha,\beta}(t|\omega) - \frac{1}{i\hbar} [\rho_{11}^{\alpha,\beta}(t) - \rho_{22}^{\alpha,\beta}(t)] \\
 &\quad \times \{V_{12}^{\alpha,\beta} - (n_d^{\alpha,\beta} (d_{12}^{\alpha,\beta})^2 / \epsilon_0 \epsilon_d) \tilde{\rho}_{12}^{\alpha,\beta}(t|\omega) - (n_d^{\beta,\alpha} d_{12}^{\alpha,\beta} d_{12}^{\beta,\alpha} / \epsilon_0 \epsilon_d) \exp[-\kappa_{\beta,\alpha}(\omega)D_0] \tilde{\rho}_{12}^{\beta,\alpha}(t|\omega)\}, \\
 \frac{d\rho_{22}^{\alpha,\beta}(t)}{dt} &= \frac{2}{\hbar} \text{Im}\{[V_{12}^{\alpha,\beta} - (n_d^{\beta,\alpha} d_{12}^{\alpha,\beta} d_{12}^{\beta,\alpha} / \epsilon_0 \epsilon_d) \exp[-\kappa_{\beta,\alpha}(\omega)D_0] [\tilde{\rho}_{12}^{\beta,\alpha}(t|\omega)]^*] \tilde{\rho}_{12}^{\alpha,\beta}(t|\omega)\}, \\
 \rho_{11}^{\alpha,\beta}(t) &= 1 - \rho_{22}^{\alpha,\beta}(t),
 \end{aligned} \tag{17}$$

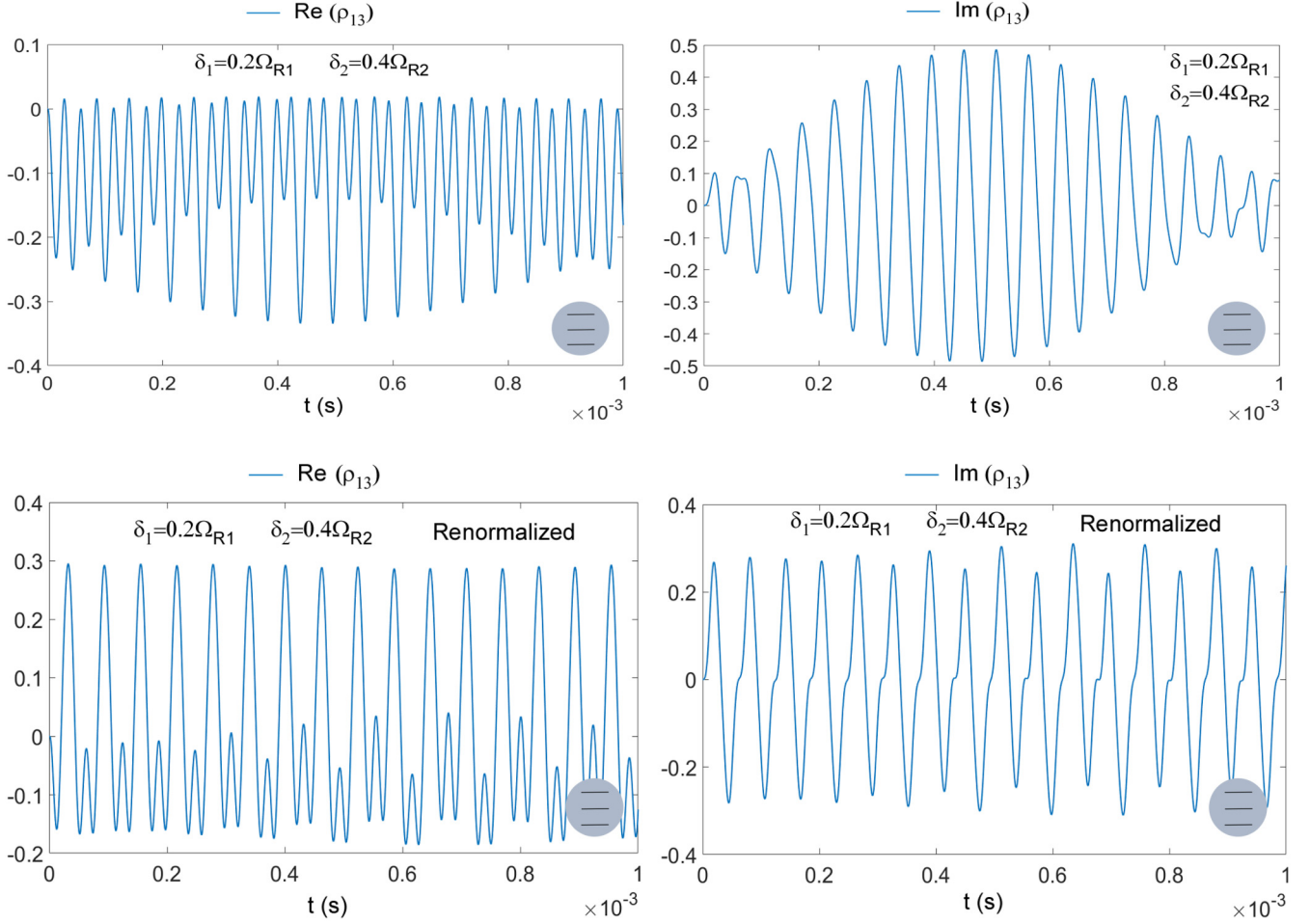


FIG. 10. Comparisons of  $\text{Re}[\tilde{\rho}_{13}(t)]$  (left) and  $\text{Im}[\tilde{\rho}_{13}(t)]$  (right) as functions of time  $t$  with (bottom) and without (top) renormalized Rabi coupling for a three-level quantum dot. Here, we have set  $\rho_{11}(0) = 1$ ,  $\rho_{22}(0) = \rho_{33}(0) = 0$  as initial conditions,  $\delta_1 = 0.2\Omega_{R1}$ , and  $\delta_2 = 0.4\Omega_{R2}$ .

where  $\alpha, \beta = 1, 2$  labels each quantum dot under the same laser field  $\mathcal{E}_L(t) = \mathcal{E}_0 \exp(i\omega t)$ ,  $d_{12}^{\alpha,\beta}$  corresponds to the dipole moment of each quantum dot, and  $D_0$  represents the center-to-center distance between two spherical quantum dots. The wave number  $\kappa_{\alpha,\beta}(\omega)$  introduced in Eq. (17) for DCI between two quantum dots is calculated as [14,30]

$$\kappa_{\alpha,\beta}(\omega) = \frac{\omega\sqrt{\epsilon_d}}{c} \sqrt{\frac{3}{\epsilon_{\alpha,\beta}(\omega) + 2}}, \quad (18)$$

which strongly depends on  $\omega$  through the dielectric function  $\epsilon_{\alpha,\beta}(\omega)$ . Furthermore,  $\epsilon_{\alpha,\beta}(\omega)$  in Eq. (18) for electrons in a spherical quantum dot takes the form [14]

$$\epsilon_{\alpha,\beta}(\omega) \approx \text{Re}[\epsilon_{\alpha,\beta}(\omega)] = 1 - \frac{n_d^{\alpha,\beta} (d_{12}^{\alpha,\beta})^2}{\epsilon_0 \epsilon_d} \left\{ \frac{\hbar\omega - (E_2^{\alpha,\beta} - E_1^{\alpha,\beta})}{[\hbar\omega - (E_2^{\alpha,\beta} - E_1^{\alpha,\beta})]^2 + (2d_{12}^{\alpha,\beta} \mathcal{E}_0)^2} \right\}, \quad (19)$$

where we have neglected the insignificant imaginary part of the dielectric function corresponding to optical loss. From Eq. (18), we easily find the LSP modes,  $\omega_{\alpha,\beta}^{sp}$ , determined by the relation  $\epsilon_{\alpha,\beta}(\omega_{\alpha,\beta}^{sp}) + 2 = 0$ , which is related to  $\kappa_{\alpha,\beta}(\omega) \rightarrow \infty$ . This leads to

$$[\omega_{\alpha,\beta}^{sp}]_{\pm} = \frac{(E_2^{\alpha,\beta} - E_1^{\alpha,\beta})}{\hbar} + \frac{n_d^{\alpha,\beta} (d_{12}^{\alpha,\beta})^2}{6\epsilon_0 \epsilon_d \hbar} \left\{ 1 \pm \sqrt{1 - \left( \frac{12\epsilon_0 \epsilon_d \mathcal{E}_0}{n_d^{\alpha,\beta} d_{12}^{\alpha,\beta}} \right)^2} \right\}, \quad (20)$$

Here, we would like to emphasize that the key aspect of the paper is to investigate the effect of Coulomb interac-

tion on transient optical response of electrons in quantum dots. The spatial arrangement of dots is simplified to the

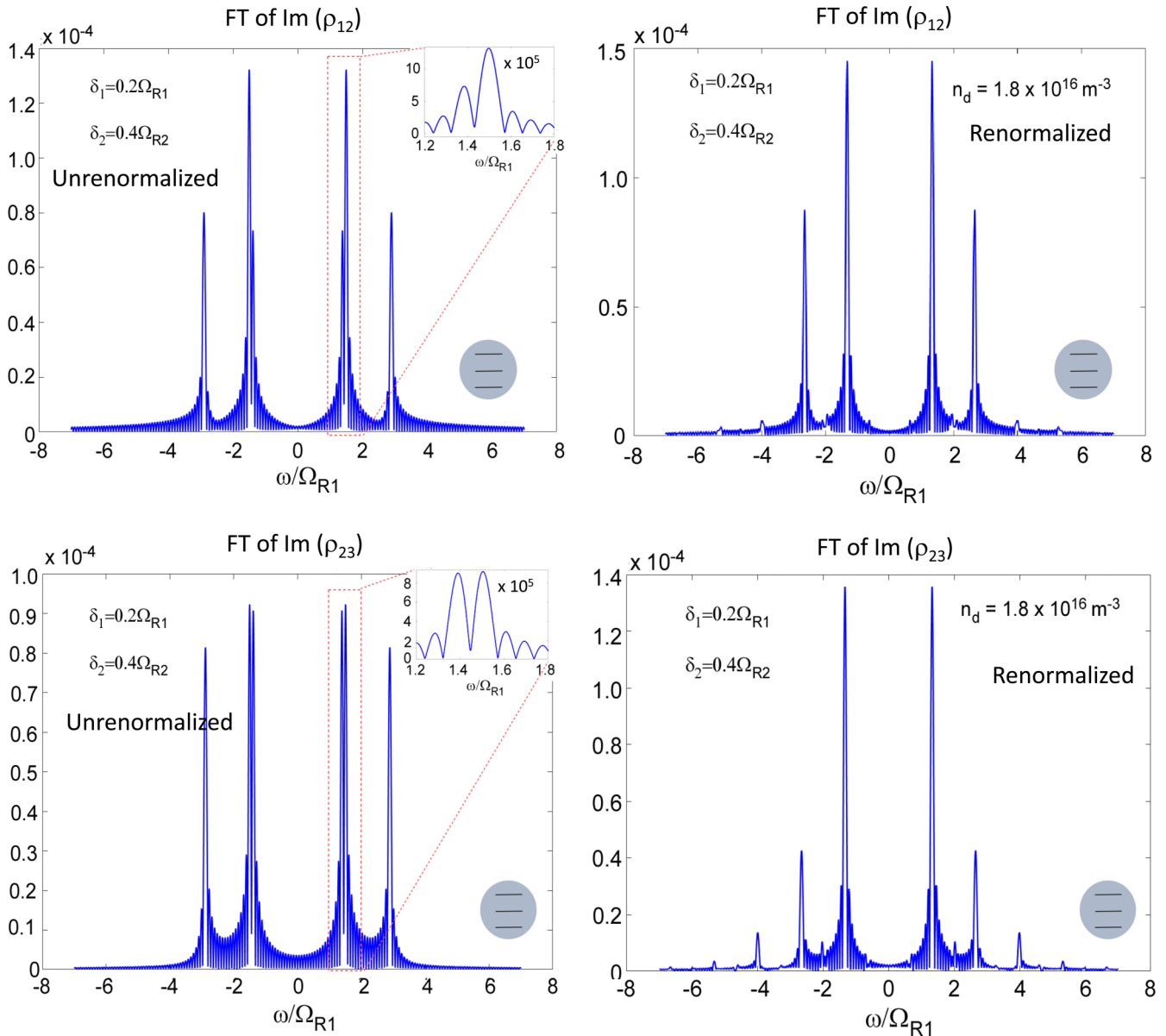


FIG. 11. Comparisons of Fourier spectra for  $\text{Im}[\bar{\rho}_{12}(t)]$  (top) and  $\text{Im}[\bar{\rho}_{23}(t)]$  (bottom) as functions of time  $t$  with bare (left) and renormalized (right) Rabi couplings for a three-level quantum dot. Here, we have set  $\rho_{11}(0) = 1$ ,  $\rho_{22}(0) = \rho_{33}(0) = 0$  as initial conditions,  $\delta_1 = 0.2\Omega_{R1}$ , and  $\delta_2 = 0.4\Omega_{R2}$ . For two unrenormalized cases, we further show insets in the left column to display fine splitting of peaks corresponding to beating features presented in right columns of Figs. 8 and 9.

physical separation. The effects of resonators and surface plasmons can be included by setting the  $\mathcal{E}$ -field profiles in the model. Specifically, let us consider a pair of optically coupled quantum dots with radius  $R$  and tangential-surface separation  $d$ . As illustrated in the bottom panel of Fig. 1, if the condition  $d \equiv D_0 - 2R \ll R$  is satisfied, we can approximately treat the interdot Coulomb interaction as one between two charge distributions confined in different parallel tangential planes separated by distance  $d$ . Therefore, the nonretarded Coulomb potential will acquire a decay factor  $\exp(-qD_0)$  for wave number  $q$  as determined from Poisson equation. In this paper, we have generalized this nonretarded interdot Coulomb interaction into a retarded one as given by Eq. (17).

For numerical calculations in Sec. IV with  $n_d^{(1)} = n_d^{(2)} = n_d$ ,  $r_0^{(1)} = r_0^{(2)} = r_0$ , and  $\kappa_1 = \kappa_2 = \kappa_\alpha$ , we set  $r_0 = 23 \text{ \AA}$  while  $n_d = 0$  and  $n_d = 1.8 \times 10^{16} \text{ m}^{-3}$  for unrenormalized and renormalized cases, respectively. Moreover, for the laser field with frequency  $\omega$ , we assume  $\Omega_R^{(1)} = \Omega_R^{(2)}/2 = \Omega_R = 1.09 \times 10^5 \text{ Hz}$  for the Rabi frequencies. The other parameters, such as  $D_0$  and  $\kappa_\alpha D_0$ , in numerical calculations will be given in the figure caption.

The calculated  $\epsilon_\alpha(\omega)$  in Eq. (19) and the inverse decay length  $\kappa_\alpha(\omega)$  in Eq. (18) as functions of  $\hbar\delta/(E_2 - E_1)$  are plotted in Fig. 13 for different values of  $\Omega_R$ . From Fig. 13, we find that the variations in both  $\epsilon_\alpha(\omega)$  and  $\kappa_\alpha(\omega)$  decrease dramatically with increasing  $\Omega_R$  due to enhanced power broadening. Here, the peak and valley in  $\epsilon_\alpha(\omega)$  correspond to the valley

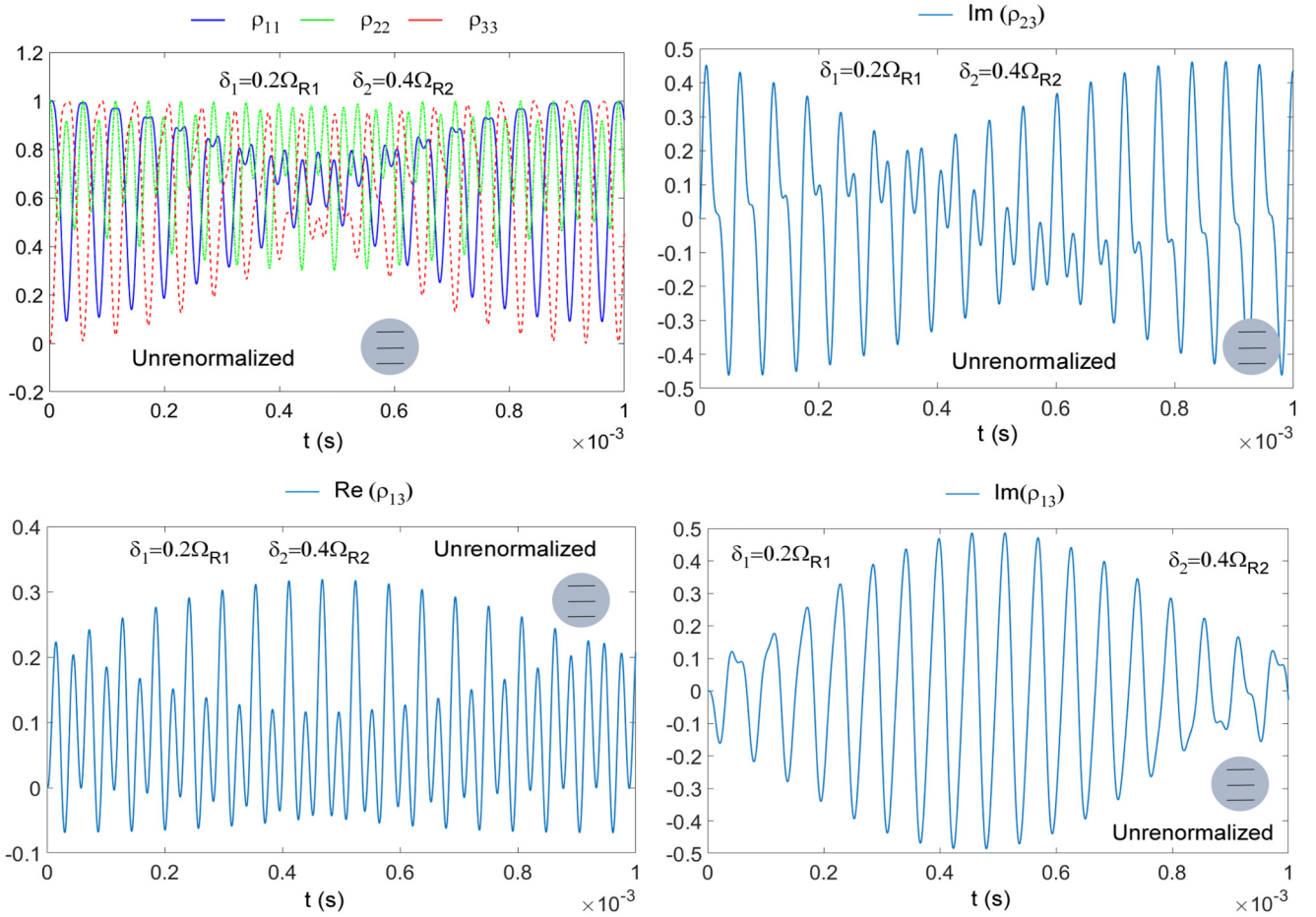


FIG. 12. Comparisons of occupations  $\rho_{11}(t)$  (blue solid),  $\rho_{22}(t)$  (green dot-dashed), and  $\rho_{33}(t)$  (red dashed) (top-left),  $\text{Im}[\bar{\rho}_{23}(t)]$  (top-right),  $\text{Re}[\bar{\rho}_{13}(t)]$  (bottom-left), and  $\text{Im}[\bar{\rho}_{13}(t)]$  (bottom-right) as functions of time  $t$  in the unrenormalized case for a three-level quantum dot. Here, we have set  $\rho_{11}(0) = \rho_{22}(0) = 1$ ,  $\rho_{33}(0) = 0$  as initial conditions,  $\delta_1 = 0.2\Omega_{R1}$ , and  $\delta_2 = 0.4\Omega_{R2}$ .

and peak of  $\kappa_\alpha(\omega)$ , as can be seen from Eq. (18). However, the peak-valley asymmetry is found for  $\kappa_\alpha(\omega)$  with a much stronger peak. Especially, the condition for exciting a spher-

ical LSP mode in Eq. (20) can be satisfied, as indicated by a steep rise in  $\kappa_\alpha(\omega)$  for a very small positive  $\hbar\delta/(E_2 - E_1)$  value, where the condition of  $\epsilon_\alpha(\omega) = -2$  can be met.

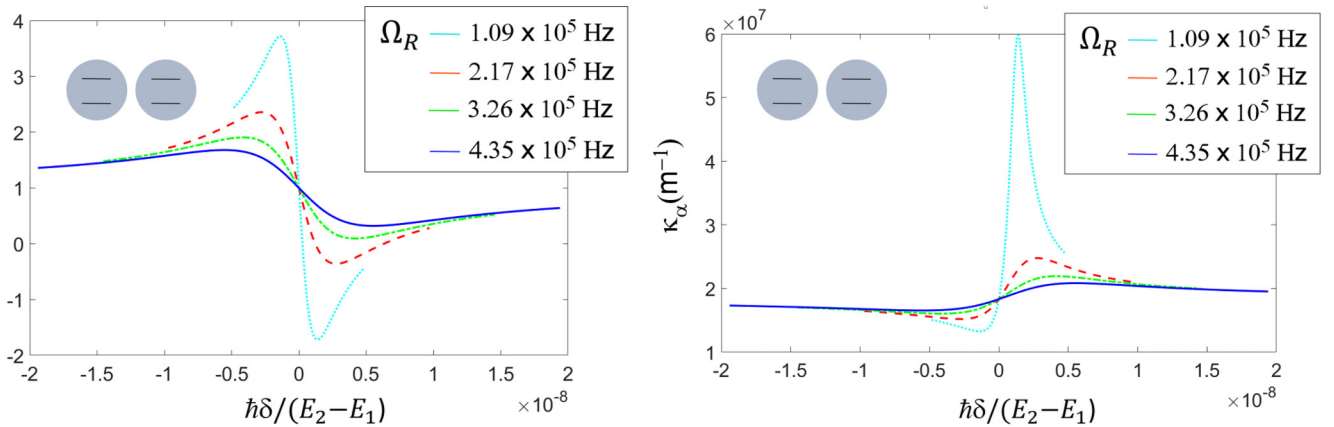


FIG. 13. Calculated dielectric function  $\epsilon_\alpha(\omega)$  (left) and inverse decay length  $\kappa_\alpha(\omega)$  (right) as functions of scaled laser detuning  $\hbar\delta/E_2 - E_1$  with  $n_d = 2.5 \times 10^{19} \text{ m}^{-3}$  and various values of Rabi frequency  $\Omega_R$  as indicated, where  $\hbar\delta = \hbar\omega - E_{21}$ . Here, Rabi frequency  $\Omega_R$  increases as  $1.09 \times 10^5 \text{ Hz}$  (cyan dotted),  $2.17 \times 10^5 \text{ Hz}$  (red dashed),  $3.26 \times 10^5 \text{ Hz}$  (green dash-dotted), and  $4.35 \times 10^5 \text{ Hz}$  (blue solid).

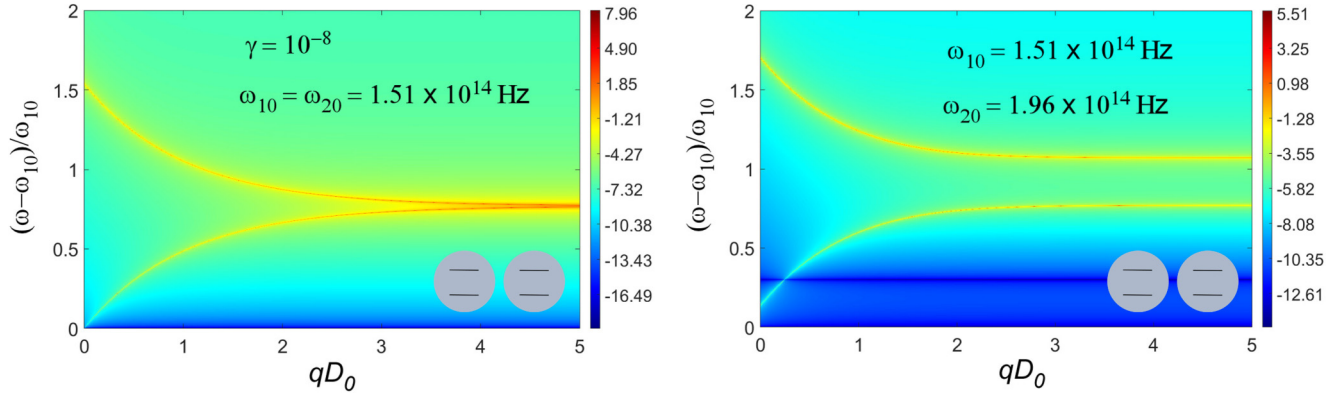


FIG. 14. Density plots of loss function in logarithmic scale for displaying scaled plasmon energies as functions of scaled wave number  $qD_0$  for near-field coupled two identical (left) or different (right) quantum dots, where  $n_d = 9.9 \times 10^{24} \text{ m}^{-3}$ ,  $\Omega_R = 1.09 \times 10^5 \text{ Hz}$ , and  $\gamma = 10^{-8}$  represents the damping of plasmon modes.

On the other hand, by considering a system containing two electromagnetically coupled (EMC) quantum dots, we can explicitly write down their nonlocal dielectric-function matrix  $\vec{\epsilon}_r(q, \omega)$ , namely

$$\vec{\epsilon}_r(q, \omega) \approx \text{Re}[\vec{\epsilon}_r(q, \omega)] = \begin{bmatrix} \epsilon_{11}(\omega) & \epsilon_{12}(q, \omega) \\ \epsilon_{21}(q, \omega) & \epsilon_{22}(\omega) \end{bmatrix}, \quad (21)$$

where  $q \geq 0$  is the wave number of LSP field, and

$$\begin{aligned} \epsilon_{11}(\omega) &= 1 - \frac{n_d^{(1)}(d_{12}^{(1)})^2}{\epsilon_0 \epsilon_d} \left\{ \frac{\hbar\omega - (E_2^{(1)} - E_1^{(1)})}{[\hbar\omega - (E_2^{(1)} - E_1^{(1)})]^2 + (2d_{12}^{(1)}\mathcal{E}_0)^2} \right\}, \\ \epsilon_{22}(\omega) &= 1 - \frac{n_d^{(2)}(d_{12}^{(2)})^2}{\epsilon_0 \epsilon_d} \left\{ \frac{\hbar\omega - (E_2^{(2)} - E_1^{(2)})}{[\hbar\omega - (E_2^{(2)} - E_1^{(2)})]^2 + (2d_{12}^{(2)}\mathcal{E}_0)^2} \right\}, \\ \epsilon_{12}(q, \omega) &= -\frac{n_d^{(2)}d_{12}^{(1)}d_{12}^{(2)}}{\epsilon_0 \epsilon_d} \exp(-qD_0) \left\{ \frac{\hbar\omega - (E_2^{(2)} - E_1^{(2)})}{[\hbar\omega - (E_2^{(2)} - E_1^{(2)})]^2 + (2d_{12}^{(2)}\mathcal{E}_0)^2} \right\}, \\ \epsilon_{21}(q, \omega) &= -\frac{n_d^{(1)}d_{12}^{(2)}d_{12}^{(1)}}{\epsilon_0 \epsilon_d} \exp(-qD_0) \left\{ \frac{\hbar\omega - (E_2^{(1)} - E_1^{(1)})}{[\hbar\omega - (E_2^{(1)} - E_1^{(1)})]^2 + (2d_{12}^{(1)}\mathcal{E}_0)^2} \right\}, \end{aligned} \quad (22)$$

while  $\text{Det}[\vec{\epsilon}_r(q, \omega)] = 0$  provides us with coupled nonlocal-plasmon modes  $\omega = \Omega_{\pm}(q)$ .

We present density plots in Fig. 14 for comparison of the loss function  $\gamma/\{|\text{Det}[\vec{\epsilon}_r(q, \omega)]|^2 + \gamma^2\}$  with respect to two either identical ( $\omega_{10} = \omega_{20}$ ) or different ( $\omega_{10} \neq \omega_{20}$ ) quantum dots, where  $\hbar\omega_{\alpha 0} \equiv E_2^{(\alpha)} - E_1^{(\alpha)}$  and very small  $\gamma > 0$  has been introduced to represent the damping of plasmon modes. For two identical quantum dots in the left panel, we find a low-energy out-of-phase acousticlike plasmon mode  $\Omega_-(q)/\omega_0$  with gapless-linear dispersion within the strong-coupling regime  $qD_0 \ll 1$ , as well as a high-energy in-phase opticlike plasmon mode  $\Omega_+(q)/\omega_0$  with an energy gap for  $q \rightarrow 0$ . For the weak-coupling regime  $qD_0 \gg 1$ , on the other hand, the energy splitting between these two plasmon modes  $\Omega_{\pm}(q)$  approaches zero, as seen from the left panel. In the right panel for two different quantum dots, however, the energies of these two plasmon modes  $\Omega_{\pm}(q)/\omega_0$  are pushed away, and meanwhile, a gap appears for  $\Omega_-(q)$  even when  $q \rightarrow 0$ , in contrast to the low-energy acousticlike plasmon mode in the left panel. Moreover, the splitting between

two plasmon modes  $[\Omega_+(q) - \Omega_-(q)]$  remains as a constant for  $qD_0 \gg 1$ .

Similar to the discussions in Sec. III on indirect transition of electrons by quantum interference in a three-level quantum dot, we know from Eq. (17) that similar phenomenon will occur in the case of EMC quantum dots, in which the finite occupation  $\rho_{22}^{\beta}(t) > 0$  for a directly pumped quantum dot with  $V_{12}^{\beta} \neq 0$  can lead to a finite occupation  $\rho_{22}^{\alpha}(t) > 0$  for an unpumped quantum dot with  $V_{12}^{\alpha} \equiv 0$  through near-field coupling between these two quantum dots. Such a phenomenon can be verified by the appearance of a finite tunneling current through this separately contacted unpumped quantum dot. For this two-dot system, the unpumped (off) state can switch to an isolated one-dot excited (partial-open) state, if the other quantum dot sits at the field node and the interdot near-field coupling can be ignored. Moreover, the same off state can also switch to coupled two-dot excited (full-open) state with strong interdot near-field coupling to the other unpumped dot. Such a switching process can be sensitively controlled by frequency detuning of an incident laser field.

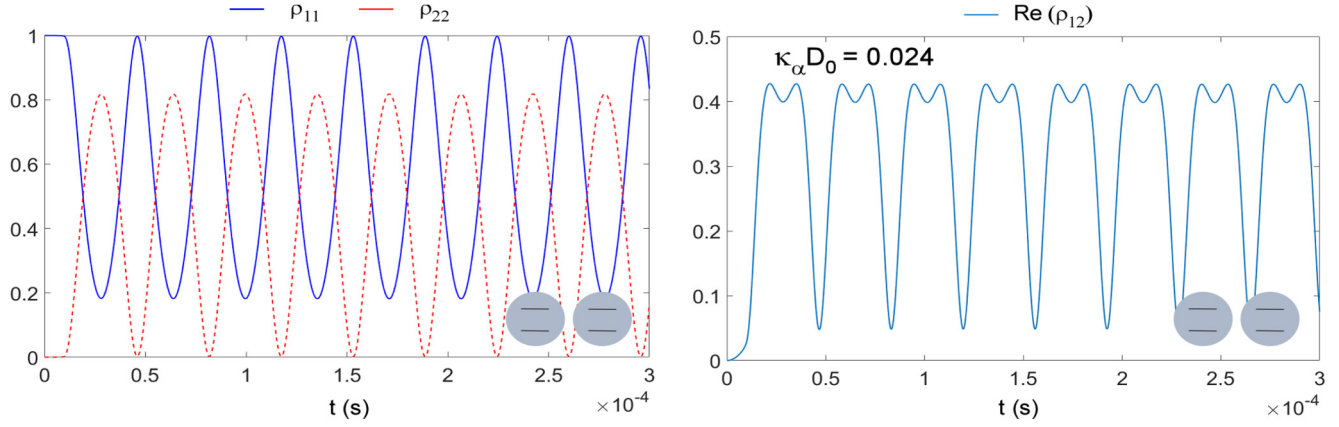


FIG. 15. Calculated  $\rho_{11}(t)$  (blue solid) and  $\rho_{22}(t)$  (red dashed) as functions of time  $t$  (left) and  $\text{Re}[\tilde{\rho}_{12}(t | \omega)]$  (right) as a function of  $t$  within the rotating-wave frame for the renormalized case. Here, two identical dots are illuminated by the same incident laser. We have set  $n_d = 1.8 \times 10^{16} \text{ m}^{-3}$ ,  $D_0 = 5 \text{ nm}$ ,  $\kappa_\alpha D_0 = 0.0242$  for a selected  $\hbar\delta$  value corresponding to  $\Omega_R = 1.09 \times 10^5 \text{ Hz}$ , and the enhanced-amplitude Rabi oscillations in the left panel can be seen clearly for EMC dots.

The selection of a large decay length can be fulfilled by a positive but very small laser-frequency detuning  $\hbar\delta$ , as seen from the right panel of Fig. 13. The increased Rabi-oscillation amplitudes for  $\rho_{11}(t)$  and  $\rho_{22}(t)$ , as well as the SFTOR in  $\text{Re}[\tilde{\rho}_{12}(t | \omega)]$ , are also expected for small  $\hbar\delta$ , as displayed in both panels of Fig. 5. Here, we present comparisons in Figs. 15 and 16 for the renormalized case of two identical quantum dots under the same laser irradiation, where these two dots are electromagnetically coupled to each other by an induced evanescent field. For a stronger interdot coupling in Fig. 15, the smaller selected  $\hbar\delta$  value leads to large-amplitude Rabi oscillations in both  $\rho_{11}(t)$  and  $\rho_{22}(t)$  as seen in the left panel, which are further accompanied by the appearance of doubly split peaks for  $\text{Re}[\tilde{\rho}_{12}(t | \omega)]$  in the right panel due to enhanced Coulomb interaction between electrons in different quantum dots. As the interdot coupling is slightly reduced in Fig. 16 with a shorter decay length at a relatively large selected  $\hbar\delta$  value, the Rabi-oscillation amplitudes of  $\rho_{11}(t)$  and  $\rho_{22}(t)$  in its left panel decrease greatly due to weakened

interdot Coulomb interaction between electrons. In addition, the nonlinear doubly split peak in  $\text{Re}[\tilde{\rho}_{12}(t | \omega)]$  disappears as can be verified from the right panel of Fig. 16.

We know the spatial distribution of a laser field within an optical cavity is inhomogeneous and can be controlled by the cavity length under the resonance condition. Therefore, the strength of a laser field acting on a quantum dot will depend on its specific position inside the cavity. To simulate this field-distribution effect, we take  $\Omega_R^{(1)} = \Omega_R^{(2)}/2 = 1.09 \times 10^5 \text{ Hz}$  in Figs. 17 and 18.

When the field coupling between two dots is strong, for a relatively smaller separation between two quantum dots as assumed in Fig. 17, we observe a new very slow ( $\sim |\Omega_R^{(1)} - \Omega_R^{(2)}|/2$ ) but very strong amplitude modulation for  $\text{Re}[\tilde{\rho}_{12}^{(1)}(t | \omega)]$  in the right panel, which is superposed on very fast oscillations ( $\sim |\Omega_R^{(1)} + \Omega_R^{(2)}|/2$ ) with respect to time. The same amplitude modulation also appears in the left panel for both  $\rho_{11}^{(1)}(t)$  and  $\rho_{22}^{(1)}(t)$  but having a much smaller magnitude.

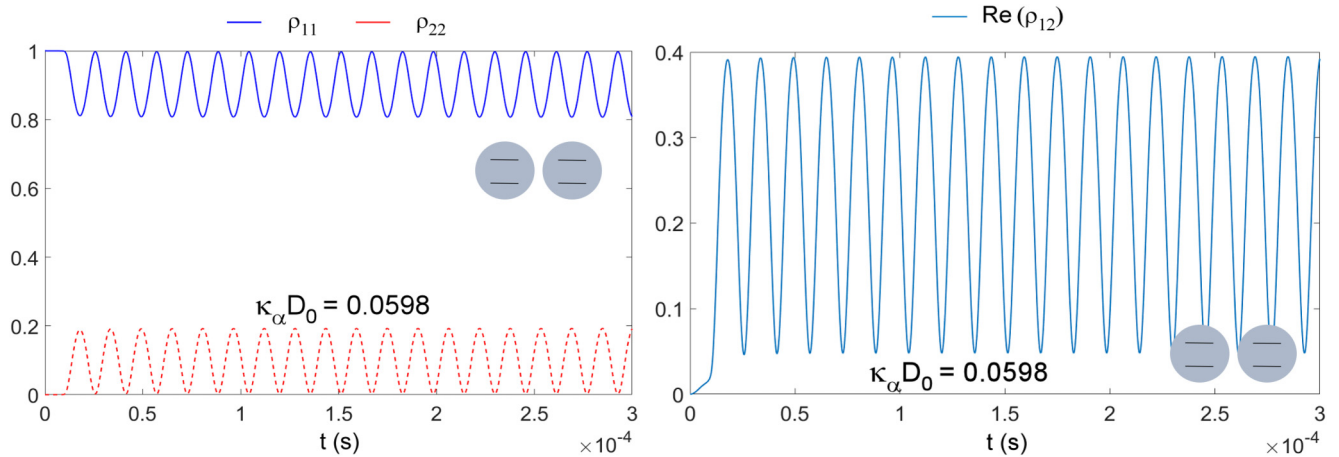


FIG. 16. Calculated  $\rho_{11}(t)$  (blue solid) and  $\rho_{22}(t)$  (red dashed) as functions of time  $t$  (left) and  $\text{Re}[\tilde{\rho}_{12}(t | \omega)]$  (right) as a function of  $t$  within the rotating-wave frame for the renormalized case. Here, we have set  $n_d = 4.1 \times 10^{16} \text{ m}^{-3}$  and  $D_0 = 5 \text{ nm}$  for two identical dots,  $\kappa_\alpha D_0 = 0.0598$  for a selected  $\hbar\delta$  value corresponding to  $\Omega_R = 1.09 \times 10^5 \text{ Hz}$ , and the reduced-amplitude Rabi oscillations in the left panel can be seen clearly for decoupled dots.

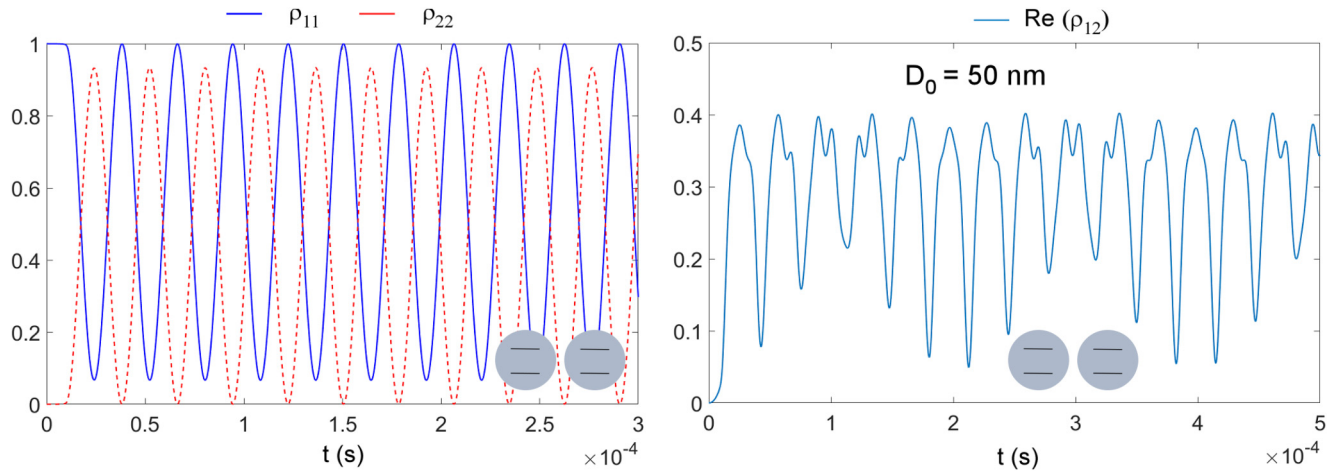


FIG. 17. Calculated  $\rho_{11}^{(1)}(t)$  (blue solid) and  $\rho_{22}^{(1)}(t)$  (red dashed) as functions of time  $t$  (left) and real part of the quantum coherence  $\text{Re}[\tilde{\rho}_{12}^{(1)}(t|\omega)]$  (right) as a function of  $t$  within the rotating-wave frame for the renormalized case. Here, two dots are illuminated by laser fields with different strengths, i.e.,  $\Omega_R^{(1)} = \Omega_R^{(2)}/2 = 1.09 \times 10^5$  Hz. We have set  $n_d = 1.8 \times 10^{16} \text{ m}^{-3}$ ,  $D_0 = 50 \text{ nm}$ ,  $\kappa_\alpha D_0 = 0.92$  for two selected  $\hbar\delta^{(1,2)}$  values corresponding to  $\Omega_R^{(1,2)}$ , and strong variations in the amplitude of  $\text{Re}[\tilde{\rho}_{12}^{(1)}(t|\omega)]$  in the right panel can be seen clearly for EMC dots.

Meanwhile, the low-frequency amplitude modulation in the right panel is further accompanied by the occurrence of asymmetric SFTORs with switching peak strength, in contrast to the symmetric doubly split peaks found in the right panel of Fig. 15.

As the interdot separation  $D_0$  increases from 50 nm to 150 nm in Fig. 18, however, the interdot coupling is expected to be reduced dramatically for a fixed decay length as in Fig. 17. As a result, the amplitude modulation for  $\text{Re}[\tilde{\rho}_{12}^{(1)}(t|\omega)]$  in the right panel becomes weakened, and simultaneously, almost no sign of amplitude modulation can be seen in the left panel for occupations  $\rho_{11}^{(1)}(t)$  and  $\rho_{22}^{(1)}(t)$ . Additionally, the asymmetric doubly split peaks observed in the right panel of Fig. 17 has largely been symmetrized in the right panel of Fig. 18 but still acquiring slightly varied depths in the profile of split peaks of SFTORs. The amplitude-modulation effect in  $\text{Re}[\tilde{\rho}_{12}^{(1)}(t|\omega)]$  is found weakened for a

weaker interdot coupling, and the modulation period becomes larger.

## V. CONCLUSIONS AND REMARKS

In conclusion, we have employed the DMT for exploring coherent electron dynamics, namely, occupations as well as directly or indirectly induced quantum coherence under laser irradiation in both single- and double-quantum-dot systems. The inclusion of renormalization to Rabi coupling results from the SCIDF of photoexcited electrons, which corresponds to DCIs between two electrons within the same or different quantum dots. Based on the evanescent LSP-field description, the near-field coupling, relating to interdot quantum-mechanical DCI, has been introduced and leads to second-order sum- and difference-frequency transient optical responses of electrons within dual EMC quantum dots

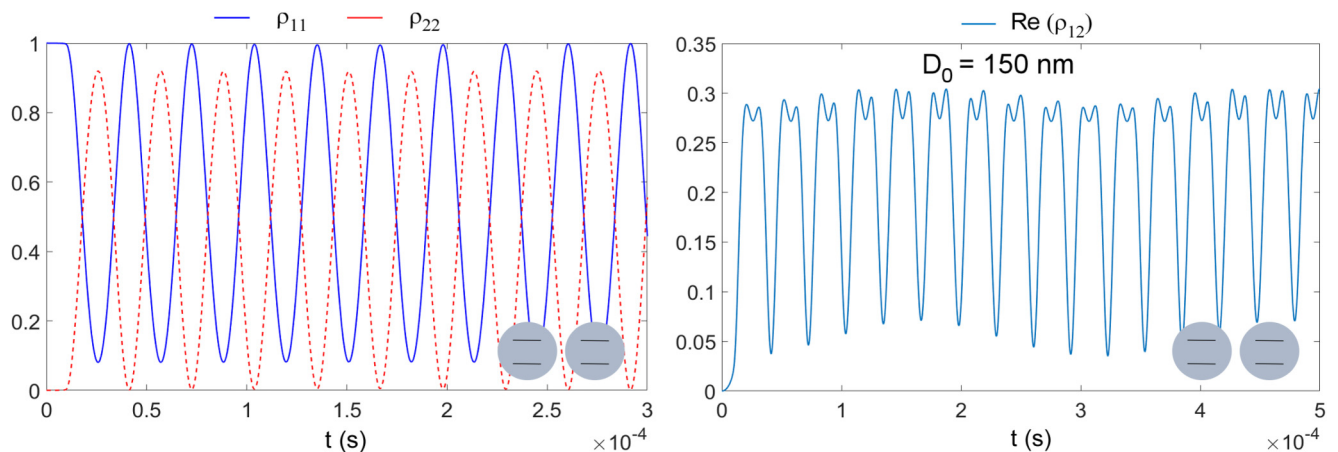


FIG. 18. Calculated  $\rho_{11}^{(1)}(t)$  (blue solid) and  $\rho_{22}^{(1)}(t)$  (red dashed) as functions of time  $t$  (left) and  $\text{Re}[\tilde{\rho}_{12}^{(1)}(t|\omega)]$  (right) as a function of  $t$  within the rotating-wave frame for the renormalized case. Here, two dots are illuminated by laser fields with different strengths, i.e.,  $\Omega_R^{(1)} = \Omega_R^{(2)}/2 = 1.09 \times 10^5$  Hz. We have set  $n_d = 1.8 \times 10^{16} \text{ m}^{-3}$ ,  $D_0 = 150 \text{ nm}$ ,  $\kappa_\alpha D_0 = 2.75$  for two selected  $\hbar\delta^{(1,2)}$  values corresponding to  $\Omega_R^{(1,2)}$ , and weak variations in the amplitude of  $\text{Re}[\tilde{\rho}_{12}^{(1)}(t|\omega)]$  in the right panel can be seen clearly for decoupled dots.

in a two-level model. For a three-level quantum dot, we have further explored the quantum interference between two consecutive laser-induced quantum coherence and its unique effect on indirectly induced quantum coherence under the irradiation of dual laser beams.

Although the occupations of electronic states, corresponding to two energy levels of a quantum dot, only produces a normal Rabi oscillation under a continuous laser-field excitation, they demonstrate a unique and fully controllable switching between these occupations under femtosecond-laser-frequency-comb excitations. In addition, by introducing a near-field coupling for two close-by quantum dots, one can selectively engineer the phase entanglement of these two laser-dressed quantum dots, which is expected to be very important and useful for facilitating quantum communication,

quantum sensing and ultrasensitive quantum-dot photodetectors, as well as dramatically enhancing the electro-optical response in many infrared optoelectronics devices.

#### ACKNOWLEDGMENTS

X.L. acknowledges the support from the Air Force Research Lab Summer Faculty Fellowship Program sponsored by AFOSR and AFSOR DURIP program (Grant No. FA9550-18-1-0444). D.H. would like to acknowledge the financial supports from the Laboratory University Collaboration Initiative (LUCI) program and from the Air Force Office of Scientific Research (AFOSR). S.F. acknowledges the support of an AFOSR MURI project. (Grant No. FA9550-17-1-0002).

- 
- [1] W. Kohn and L. Sham, Self-consistent equations including exchange and correlation effects, *Phys. Rev.* **140**, A1133 (1965).
- [2] H. Haug and S. W. Koch, *Quantum Theory of the Optical and Electronic Properties of Semiconductors* (World Scientific, Singapore, 2009), 4th ed.
- [3] H. Haug and A.-P. Jauho, *Quantum Kinetics in Transport and Optics of Semiconductors* (Springer-Verlag, Berlin, 1996).
- [4] S. W. Koch, *Microscopic Theory of Semiconductors: Quantum Kinetics, Confinement and Lasers* (World Scientific, Singapore, 1995).
- [5] W. W. Chow, Stephan W. Koch, and Murray Sargent III, *Semiconductor-Laser Physics* (Springer-Verlag, Berlin, 1994).
- [6] G. Gumbs and D. H. Huang, *Properties of Interacting Low-Dimensional Systems* (Wiley-VCH Verlag GmbH, New York, 2011).
- [7] J. R. Gulley and D. H. Huang, Self-consistent quantum-kinetic theory for interplay between pulsed-laser excitation and nonlinear carrier transport in a quantum-wire array, *Opt. Expr.* **27**, 17154 (2019).
- [8] M. Lindberg and S. W. Koch, Effective Bloch equations for semiconductors, *Phys. Rev. B* **38**, 3342 (1988).
- [9] M. Kira and S. W. Koch, Many-body correlations and excitonic effects in semiconductor spectroscopy, *Progr. Quant. Electr.* **30**, 155 (2006).
- [10] R.P. Smith, J.K. Wahlstrand, A.C. Funk, R.P. Mirin, S.T. Cundiff, J.T. Steiner, M. Schafer, M. Kira, and S.W. Koch, Extraction of Many-Body Configurations from Nonlinear Absorption in Semiconductor Quantum Wells, *Phys. Rev. Lett.* **104**, 247401 (2010).
- [11] G. Khitrova, H. M. Gibbs, M. Kira, S. W. Koch, and A. Scherer, Vacuum Rabi splitting in semiconductors, *Nature Phys.* **2**, 81 (2006).
- [12] G. Khitrova, H. M. Gibbs, F. Jahnke, M. Kira, and S. W. Koch, Nonlinear optics of normal-mode-coupling semiconductor microcavities, *Rev. Mod. Phys.* **71**, 1591 (1999).
- [13] Y. Z. Hu, M. Lindberg, and S. W. Koch, Theory of optically excited intrinsic semiconductor quantum dots, *Phys. Rev. B* **42**, 1713 (1990).
- [14] D. H. Huang, M. Easter, G. Gumbs, A. A. Maradudin, S.-Y. Lin, D. A. Cardimona, and X. Zhang, Controlling quantum-dot light absorption and emission by a surface-plasmon field, *Opt. Expr.* **22**, 27576 (2014).
- [15] A. Iurov, D. H. Huang, G. Gumbs, W. Pan, and A. A. Maradudin, Effects of optical polarization on hybridization of radiative and evanescent field modes, *Phys. Rev. B* **96**, 081408(R) (2017).
- [16] D. A. Cardimona and D. H. Huang, Connection of off-diagonal radiative-decay coupling to electromagnetically induced transparency and amplification without inversion in a three-level atomic system, *Phys. Rev. A* **65**, 033828 (2002).
- [17] S. E. Harris, Lasers without Inversion: Interference of Lifetime-Broadened Resonances, *Phys. Rev. Lett.* **62**, 1033 (1989).
- [18] J. Mompert and R. Corbalan, Lasing without inversion, *J. Opt. B: Quantum Semiclass. Opt.* **2**, R7 (2000).
- [19] M. O. Scully and M. S. Zubairy, *Quantum Optics* (Cambridge University Press, Cambridge, 1997).
- [20] Y. Zhao, D. H. Huang, and C. Wu, Electric-field-induced quantum coherence of the intersubband transition in semiconductor quantum wells, *Opt. Lett.* **19**, 816 (1994).
- [21] K. J. Boller, A. Imamoglu, and S. E. Harris, Observation of Electromagnetically Induced Transparency, *Phys. Rev. Lett.* **66**, 2593 (1991).
- [22] J. H. Eberly, M. L. Pons, and H. R. Haq, Dressed-Field Pulses in an Absorbing Medium, *Phys. Rev. Lett.* **72**, 56 (1994).
- [23] D. H. Huang and D. A. Cardimona, Effects of off-diagonal radiative-decay coupling on electron transitions in resonant double quantum wells, *Phys. Rev. A* **64**, 013822 (2001).
- [24] Y. Rostovtsev, O. Kocharovskaya, G. R. Welch, and M. O. Scully, Slow, Ultraslow, Stored, and Frozen Light, *Opt. & Photon. News* **13**, 44 (2002).
- [25] V. N. Bagratashvili, V. S. Letokhov, A. A. Makarov, and E. A. Ryabov, Multiple-photon infrared laser photophysics and photochemistry. II, *Laser Chem.* **4**, 1 (1983).
- [26] Y. R. Shen, *The Principles of Nonlinear Optics*, 1st ed. (Wiley, New York, 2002).
- [27] V. M. Agranovich and A. A. Maradudin, *Surface Excitations* (North-Holland, Amsterdam, 1984).
- [28] J. D. Jackson, *Classical Electrodynamics*, 3rd ed. (John Wiley & Sons, New Jersey, 1999).

- [29] D. H. Huang and P. R. Antoniewicz, Coupled tunneling plasmon excitations in a planar array of quantum dots, *Phys. Rev. B* **43**, 2169 (1991-II).
- [30] Heinz Raether, *Surface Plasmons on Smooth and Rough Surfaces and on Gratings* (Springer-Verlag, Berlin, 1988).
- [31] M. Minkov, D. Gerace, and S. Fan, Doubly resonant  $\chi^{(2)}$  nonlinear photonic crystal cavity based on a bound state in the continuum, *Optica* **6**, 1039 (2019).
- [32] J. R. Piper and S. Fan, Broadband Absorption enhancement in solar cells with an atomically thin active layer, *ACS Photon.* **3**, 571 (2016).
- [33] M. Matthews, F. Morales, A. Patas, A. Lindinger, J. Gateau, N. Berti, S. Hermelin, Jérôme Kasparian, M. Richter, T. Bredtmann, O. Smirnova, J.-P. Wolf, and M. Ivanov, Amplification of intense light fields by nearly free electrons, *Nature Phys.* **14**, 695 (2018).
- [34] D. E. Westmoreland, K. P. McClelland, K. A. Perez, J. C. Schwabacher, Z. Zhang, and E. A. Weiss, Properties of quantum dots coupled to plasmons and optical cavities, *J. Chem. Phys.* **151**, 210901 (2019).
- [35] K. Edamatsu, T. Itoh, S. Hashimoto, B. P. Zhang, and Y. Segawa, Micro-photoluminescence spectroscopy of CuCl quantum dots in thin NaCl crystals, *J. Lumin.* **87–89**, 387 (2000).
- [36] M. Hauser, J. Smoliner, C. Eder, G. Ploner, G. Strasser, and E. Gornik, Single quantum dots as scanning tunneling microscope tips, *Superlattices Microstruct.* **20**, 623 (1996).
- [37] A. E. Siegman, *Lasers* (University Science Books, Mill Valley, 1986).
- [38] Y. Shi, Q. Lin, M. Minkov, and S. Fan, Nonreciprocal optical dissipation based on direction-dependent Rabi splitting, *IEEE J. Sel. Top. Quantum Electron.* **24**, 3500107 (2018).
- [39] J. L. Hall, Nobel Lecture: Defining and measuring optical frequencies, *Rev. Mod. Phys.* **78**, 1279 (2006).
- [40] T. W. Hänsch, Nobel Lecture: Passion for precision, *Rev. Mod. Phys.* **78**, 1297 (2006).
- [41] P. Michler, A. Kiraz, C. Becher, W. V. Schoenfeld, P. M. Petroff, L. Zhang, E. Hu, and A. Imamoglu, A quantum dot single-photon turnstile device, *Sci.* **290**, 2282 (2000).
- [42] G. Juska, V. Dimastrodonato, L. O. Mereni, A. Gocalinska, and E. Pelucchi, Towards quantum-dot arrays of entangled photon emitters, *Nature Photon.* **7**, 527 (2013).
- [43] T. Murata, S. Asahi, S. Sanguinetti, and T. Kita, Infrared photodetector sensitized by InAs quantum dots embedded near an  $\text{Al}_{0.3}\text{Ga}_{0.7}\text{As}/\text{GaAs}$  heterointerface, *Sci. Rep.* **10**, 11628 (2020).
- [44] G. Gu, N. Mojaverian, J. Vaillancourt, and X. Lu, Surface plasmonic resonance induced near-field vectors and their contribution to quantum dot infrared photodetector enhancement, *J. Phys. D: Appl. Phys.* **47**, 435106 (2014).
- [45] P. M. Alsing, D. H. Huang, D. A. Cardimona, and T. Apostolova, Interplay between Coulomb interaction and quantum interference in three-level resonant asymmetric double quantum wells, *Phys. Rev. A* **68**, 033804 (2003).
- [46] D. H. Huang and M. O. Manasreh, Intersubband transitions in strained  $\text{In}_{0.07}\text{Ga}_{0.93}\text{As}/\text{Al}_{0.40}\text{Ga}_{0.60}\text{As}$  multiple quantum wells and their application to a two-colors photodetector, *Phys. Rev. B* **54**, 5620 (1996).
- [47] S. Schmitt-Rink, D. S. Chemla, and D. A. B. Miller, Theory of transient excitonic optical nonlinearities in semiconductor quantum-well structures, *Phys. Rev. B* **32**, 6601 (1985).
- [48] D. A. B. Miller, D. S. Chemla, and S. Schmitt-Rink, Relation between electroabsorption in bulk semiconductors and in quantum wells: The quantum-confined Franz-Keldysh effect, *Phys. Rev. B* **33**, 6976 (1986).
- [49] S. Schmitt-Rink, D. A. B. Miller, and D. S. Chemla, Theory of the linear and nonlinear optical properties of semiconductor microcrystallites, *Phys. Rev. B* **35**, 8113 (1987-II).
- [50] S. Schmitt-Rink, D. S. Chemla, and H. Haug, Nonequilibrium theory of the optical Stark effect and spectral hole burning in semiconductors, *Phys. Rev. B* **37**, 941 (1988).
- [51] S.-L. Chuang, S. Schmitt-Rink, D. A. B. Miller, and D. S. Chemla, Exciton Green's-function approach to optical absorption in a quantum well with an applied electric field, *Phys. Rev. B* **43**, 1500 (1991).
- [52] D. S. Chemla, D. A. B. Miller, and S. Schmitt-Rink, Generation of Ultrashort Electrical Pulses through Screening by Virtual Populations in Biased Quantum Wells, *Phys. Rev. Lett.* **59**, 1018 (1987).